This is to certify that the
dissertation entitled

LOCAL STRUCTURE STUDY OF NEW
THERMOELECTRIC MATERIALS

presented by

HE LIN

has been accepted towards fulfillment
of the requirements for the

Ph.D. degree in Physics

Major Professor's Signature

12/15/06

Date

MSU is an Affirmative Action/Equal Opportunity Institution

DATE DUE	DATE DUE	DATE DUE

LOCAL STRUCTURE STUDY OF NEW THERMOELECTRIC MATERIALS

By

He Lin

A DISSERTATION

Submitted to
Michigan State University
in partial fulfillment of the requirements
for the Degree of

DOCTOR OF PHILOSOPHY

Department of Physics and Astronomy

2006

ABSTRACT

LOCAL STRUCTURE STUDY OF NEW THERMOELECTRIC MATERIALS

By

He Lin

The *atomic pair distribution function* (PDF) technique is used to study the local structure of new thermoelectric materials. The PDF is obtained via Fourier transformation of powder *total* scattering data including the important local structural information in the diffuse scattering intensities underneath, and in-between, the Bragg peaks. Having long been used to study liquids and amorphous materials, the PDF technique has been recently successfully applied to highly crystalline materials owing to the advances in modern X-ray and neutron sources and computing power.

Devices based on the thermoelectric effect hold promise for solid-state cooling and power generation but developments in materials properties are required for widespread application. Recently, the importance of nanometer-scale structures has been recognized for improving the thermoelectric properties of materials. In this work we couple the power of the PDF method for giving nano-scale structural information with the need to characterize nanostructure in a number of promising novel thermoelectric materials.

Promising Nanoclusters are found to exist in the PbTe based materials with unusual thermoelectric properties. For two series of material $AgPb_mSbTe_{m+2}$ and $(PbTe)_{1-x}(PbS)_x$ we verify the bulk nature of such nanoclusters and also determine the average chemical composition and nature of these nanoclusters. Traces of nanoclusters are also found in $Ag_{1-x}SnSb_{1+x}Te_3$ series materials.

This information is important in the effort to understand the relationship between the existence of nanoclusters and the exceptional thermoelectric properties.

To my parents, brother, cousinry, friends, and all those who once helped me To my family, friends, and all those who once helped me

Acknowledgments

When this moment come, all that happened in the last six and half years come to my mind–excitements in research, trivial things in life. But first of all that stands out is this grateful feeling towards these special people. I need to thank them all, but the words are just so limited now.

Above all, I need to express my great appreciation to my advisor, Professor Simon Billinge. Such unlimited understanding and patience he has been the source of strength for me. Simon's optimistic, positive attitude of life always cheers me up and gives me the confidence in any case. His deep insight in science and great skills in both research and people have made study and work an thorough enjoyment. No spurious words to thank Simon for the tremendous help he once gave me.

I am grateful to my thesis committee members, S. D. Mahnti, Chong-Yu Ruan, C.-P. Yuan, M. G. Kanatzidis. My highest respect to all of them. My Ph.D. research benefits a lot from collaborations with Eric Quarez, J. Androulakis, Hoang Khang. Our cooperations have been extremely efficient and smooth due to mutual interest in science.

I need to thank all of current and former post-doctors and students in our group. My research will not succeed without their help. Their unselfish spirit and contribution make our research work smooth and fast. Here I need to list them all: Emil Bozin, Pavol Juhas, Gianluca Paglia, Ahmad Masadeh, Hyunjeong Kim, Moneeb Taiseer Shatnawi, Mouath G. Shatnawi and Xiangyun Qiu. All of my success and happiness also belong to you guys.

I would like to thank Debbie Simmons and Cathy Cords who make my study here much easier with their considerate help. I also acknowledge help from Didier Wermeille, Doug Robinson for help with X-ray experiments.

My grandparents, my parents, my brother, my cousins, all of my other family members, I can not achieve this without your support. This time belongs to you.

The work at MSU benefited from support from National Science Foundation through NIRT grant DMR-0304391. X-ray data were collected at the 6IDD beam-line Advanced Photon Source (APS). Use of the APS is supported by the U.S. DOE under Contract No. W-31-109-Eng-38. The MUCAT sector at the APS is supported by the U.S. DOE under Contract No. W-7405-Eng-82.

Contents

List of Figures

List of Tables

Chapter 1

Introduction

1.1 Physics of thermoelectric materials

Thermoelectrics (TE) are an important class of technological materials that are capable of converting heat flow into electrical current, and vice versa [2, 3, 4, 5]. Modern TE materials are special types of semiconductors that, when coupled, function as a "heat pump". By applying a low voltage DC power source, heat is moved in the direction of the current (+ to -). Usually, they are used for thermoelectric modules where a single couple or many couples (to obtain larger cooling capacity) are combined. One face of the module cools down while the other heats up, and the effect is reversible. Thermoelectric cooling allows for small size and light devices, high reliability and precise temperature control, and quiet operation. Disadvantages include high prices and high operating costs, due to low energy efficiency [6].

It can be shown that the maximum efficiency of a thermoelectric device, used either to convert heat to electricity or to remove heat using electric power, is the product of the Carnot efficiency and a device dependent term that is a function of the parameter ZT, where T is temperature and Z is the thermoelectric figure of merit. The materials that are of interest for TE applications are poor thermal conductors but at the same time good electrical conductors, *i.e.*, they maximize the TE figure-

of-merit

$$ZT = \frac{S^2 T}{\kappa \rho}, \tag{1.1}$$

where S, ρ, and κ denote thermoelectric power, electrical resistivity, and thermal conductivity, respectively [6]. There is a large need for higher performance materials than those that currently exist. Much of the new materials research in the TE field is focused on finding materials with high thermoelectric figure of merit Z.

Early TE materials were Bi_2Te_3 [7] and Si-Ge [7] systems. More recently, the focus on new materials development was shifted to skutterudites[8, 9] and clathrates [10], superlattice structures [11, 12, 13, 14], and low-dimensional [15] and disordered systems [16, 17]. Currently the best TE materials are artificial multilayered semiconducting alloys with low phonon thermal conductivity and large electronic mobility [18, 11]. The misfit-layered oxides like $Ca_3Co_4O_9$ accomplish a similar effect in naturally assembled crystals that play a dual role of being a "phonon glass" and an "electron crystal" [7]. They attract now interest as candidates for high-temperature TE applications.

This thesis represents an attempt to understand the role that local structure plays in newly emerging and promising classes of TE materials based around PbTe.

1.2 Chronology of TE effect discoveries

1.2.1 The Seebeck effect

Seebeck (1770-1831) is famous for the discovery of the first thermoelectric effect [19]. The Seebeck coefficient is defined as the open circuit voltage, V, produced between two points on a conductor where a uniform temperature difference, dT of 1K exists between those points. More precisely,

$$dV = SdT, \tag{1.2}$$

or equivalently

$$E = S\nabla T, \tag{1.3}$$

where S is called the Seebeck coefficient or thermoelectric power.

1.2.2 The Peltier effect

In 1834 Peltier [20] described thermal effects at the junctions of dissimilar conductors when an electrical current flows between the materials. Peltier himself failed to fully understand the implications of his findings and it wasn't until four years later that Lenz concluded that there is heat absorption or generation at the junctions depending on the direction of current flow (see [21]). The Peltier coefficient Π represents how much heat current is carried per unit charge through a given material. When two different materials are connected to each other at two junctions and a current is flowing through the circuit, due to the different Π values, heat will transfer from one junction to the other: one junction cools off while the other heats up.

1.2.3 The Thomson effect

In 1851, Thomson [22] (later Lord Kelvin) predicted and observed experimentally the cooling or heating of a homogeneous conductor resulting from the flow of an electrical current in the presence of a temperature gradient, dT/dx. This is known as the Thomson effect. Any current-carrying conductor, with a temperature difference between two points, will either absorb or emit heat, depending on the material. If a current density J is passed through a homogeneous conductor, heat production per unit volume, q, is the usual Joule heat plus the Thomson heat:

$$q = \rho J^2 - \mu J dT/dx. \tag{1.4}$$

Here, ρ is the resistivity and μ is the Thomson coefficient.

1.2.4 The Kelvin relationship

The three thermoelectric effects above are related by the Kelvin relationships (see [23]), assumed to be valid for all thermoelectric materials. The first Kelvin (Thomson) relation connects the Peltier coefficient Π, Seebeck coefficient S and the absolute temperature T

$$\Pi = S \cdot T. \tag{1.5}$$

The second Kelvin (Thomson) relation relates the Thomson coefficient μ with the derivative of the Seebeck coefficient with regard to the temperature

$$\mu = T\frac{dS}{dT}. \tag{1.6}$$

1.3 Engineering aspects of TE physics

1.3.1 Simple overview of the Seebeck effect

In TE materials there are free carriers which carry both charge and heat. The simplest picture one can think of is that of a gas of charged particles. If the molecules are not charged, when such a gas is placed in a box with a temperature gradient, where one side is cold and the other one is hot, the gas molecules at the hot end will move faster than those at the cold end. The faster hot molecules will diffuse further than the cold molecules do, and so the cold end will have a higher density. The density gradient will cause the molecules to diffuse back to the hot end. In the steady state, the effect of the density gradient will exactly counteract the effect of the temperature gradient so there is no net flow of molecules. If the molecules are charged, the buildup of charge at the cold end will also produce a *repulsive* electrostatic force (and therefore electric potential) to push the charges back to the hot end. The electric potential produced by a temperature difference is known as the Seebeck effect and the proportionality

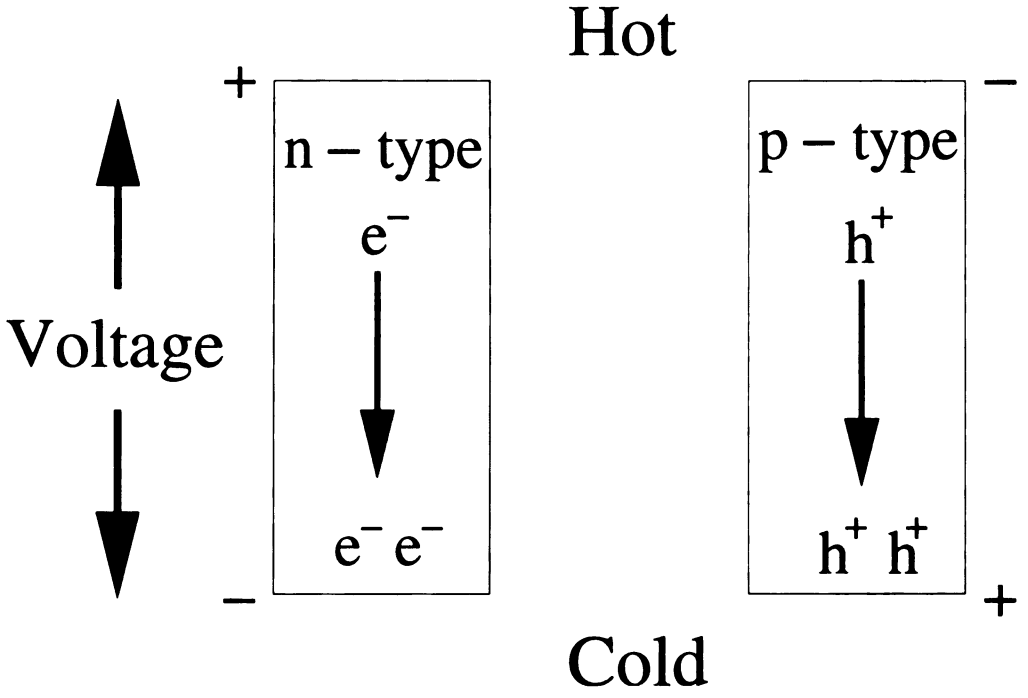

Figure 1.1: Illustration of the Seebeck effect[reproduced with the permission of Dr. Jeff Snyder] [24]

constant is called the Seebeck coefficient. If the free charges are positive (the material is p-type), positive charge will build up on the cold end which will have a positive potential. Similarly, negative free charges (n-type material) will produce a negative potential at the cold end. This is schematically illustrated in Figure 1.1.

1.3.2 TE power generation

If the hot ends of an n-type and a p-type material are electrically connected, and a load is connected across the cold ends (Figure 1.2) the voltage produced by the Seebeck effect will cause electric current to flow through the load, generating the electric power [6]. Then the following will hold

$$V = S\delta\, T, \tag{1.7}$$

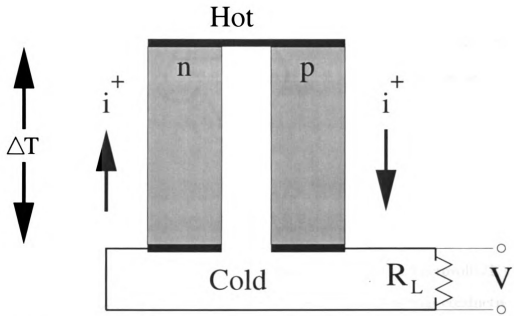

Figure 1.2: Schematic of thermoelectric power generation[reproduced with the permission of Dr. Jeff Snyder] [24]

and the resistance is given by

$$R_{load} \approx \frac{L}{\sigma A}, \tag{1.8}$$

where σ is the electrical conductivity, L/A is the ratio between the length and the cross section area of the TE elements. This further brings

$$P = IV = \frac{V^2}{R} \approx S^2 \sigma \delta T^2 \frac{A}{L} \tag{1.9}$$

$S^2\sigma$ is a property of a material known as the thermoelectric power factor. For efficient operation, high power must be produced with a minimum of heat Q. The thermal efficiency is then defined as

$$\eta = \frac{P}{Q}. \tag{1.10}$$

It can be seen then that to have a high efficiency thermoelectric generator two requirements must be met: large δT to increase the Carnot factor, and a large thermoelectric figure of merit ZT. Increasing ZT is the focus of all contemporary TE materials de-

velopment and increasing δT represents a goal of generator design.

The thermoelectric figure of merit, ZT, characterizes the efficiency of a TE material at operating temperature T. Z is a property of a material defined as

$$Z = \frac{S^2}{\kappa\rho}, \tag{1.11}$$

where

$$\rho = \frac{1}{\sigma}. \tag{1.12}$$

Here, S is the Seebeck coefficient of the material (measured in microvolts/K), σ is the electrical conductivity of the material and κ is the total thermal conductivity of the material.

1.3.3 Utilizing Peltier cooling

If an electrical current is introduced in a TE material by an external electric potential (Figure 1.3) then the heat can be forced to flow from one end to the other. The coefficient of performance and the maximum temperature drop that can be achieved is again related to the efficiency of a TE material through the TE figure of merit ZT.

1.3.4 Using Thomson effect to predict Seebeck coefficient

The second Kelvin (Thomson) relation provides a connection between the Thomson coefficient μ and the derivative of the Seebeck coefficient with respect to temperature:

$$\mu = T\frac{dS}{dT}. \tag{1.13}$$

By measuring the change in bulk heating as the current direction is reversed for fixed temperature gradient, we can determine the temperature derivative of the thermopower, and therefore compute the value of S at high temperatures, given its low-

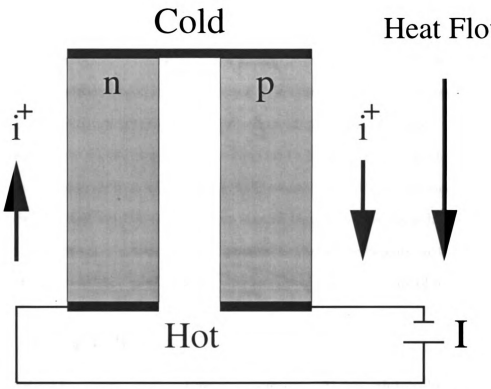

Figure 1.3: Peltier Cooling[reproduced with the permission of Dr. Jeff Snyder] [24]

temperature value.

1.4 Evolution of TE materials

It was in 1909 [25] and 1911 [26] when Altenkirch showed that good thermoelectric materials should possess large Seebeck coefficients, high electrical conductivity and low thermal conductivity. A high electrical conductivity is necessary to minimize the Joule heating, whilst a low thermal conductivity helps to retain heat at the junctions and maintain a large temperature gradient. These three properties were later embodied in the so-called figure-of-merit, Z. Since Z *varies* with temperature, a useful dimensionless figure-of-merit can be defined through ZT, as mentioned earlier.

1.4.1 Metals

Although the properties favored for good thermoelectric materials were known, the advantages of semiconductors as thermoelectric materials were neglected and research continued to focus on metals and metal alloys in the early TE days. These materials however have a constant ratio of electrical to thermal conductivity (Widemann-Franz-Lorenz law) so it is not possible to increase one without increasing the other. Metals best suited for TE applications should therefore possess a high Seebeck coefficient. Unfortunately most metals possess Seebeck coefficients in the order of 10 microvolts/K, resulting in generating efficiencies of only fractions of a percent [7].

1.4.2 Semiconductors

It was during the 1920's that the development of synthetic semiconductors with Seebeck coefficients in excess of 100 microvolts/K increased interest in TE field. At that time it was not apparent that the semiconductors were *superior* TE materials due to their higher (and hence more favorable) ratio of the electrical conductivity to thermal conductivity, compared to that of metals.

1.4.3 Pioneer work of A. F. Ioffe

As early as 1929 when very little was known about semiconductors, Abram Fedorovich Ioffe (1880-1960) showed that a thermoelectric generator utilizing semiconductors could achieve a conversion efficiency of 4 percent, with further possible improvement in its performance. By the 1950's, Ioffe and his colleagues [27] had developed the theory of thermoelectric conversion, which forms the basis of all modern thermoelectric theories.

1.4.4 Further developments and current efforts

By the late 1950's and early 1960's, a large number of semiconductor materials were investigated. Some of the materials emerged with ZT values significantly higher than in metals or metal alloys. Research focused on developing materials with high figure-of-merit values over relatively narrow temperature ranges, because no single compound semiconductor can exhibit a uniform high figure-of-merit over a wide temperature range. Of the great number of materials investigated, those based on bismuth tellurium, lead telluride and silicon-germanium alloys emerged as the best for operating temperatures of about 450 K, 900 K and 1400 K respectively [3].

In more recent days the research on developing high performance TE materials is focused in three main directions [3]: (a) superlattices and nanowires aiming at increasing S, and reducing κ, (b) utilizing nonequilibrium effect aiming to decouple electron and phonon transport, and (c) bulk nanomaterial synthesis.

One of the more promising avenues in synthesizing bulk materials with enhanced TE properties is based around PbTe class of materials that appear to contain nano-inhomogeneities whose role for TE properties is not fully understood. Investigation of the *local* structure of materials based on lead telluride, and the role that it plays in the TE properties is the subject of this thesis.

1.5 Engineering of novel TE materials - principles and examples

From the definition of the TE figure of merit provided earlier one can conclude that a material with a large thermoelectric power factor and therefore high ZT, needs to have a large Seebeck coefficient (found in low carrier concentration semiconductors or insulators) and a large electrical conductivity (found in high carrier concentration metals). The TE power factor exhibits maximum somewhere between metal and

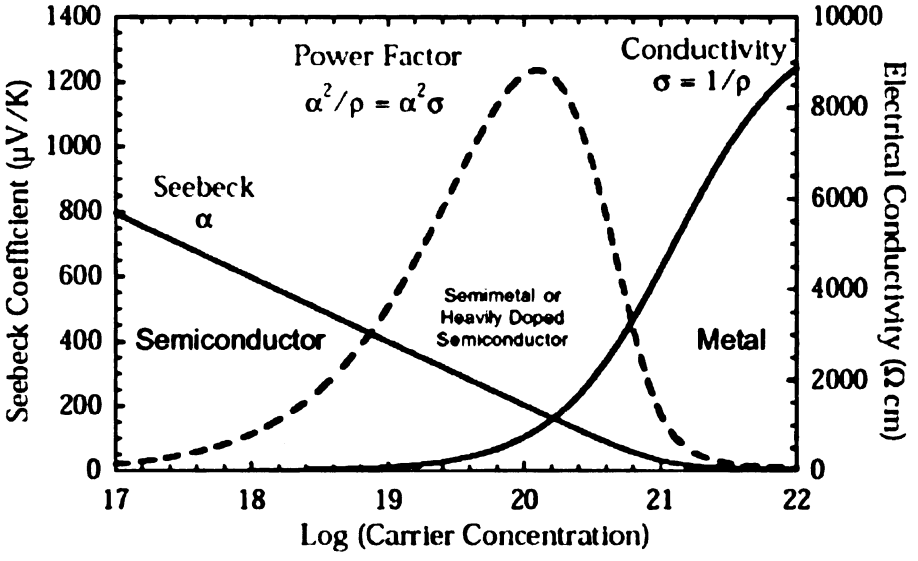

Figure 1.4: Seebeck coefficient, electrical conductivity, and power factor vs. carrier concentration [reproduced with the permission of Dr. Jeff Snyder] [24][Most images in this thesis are presented in color.]

semiconductor (Figure 1.4). Good TE materials are typically heavily doped semiconductors or semimetals with carrier concentrations between 10^{19} and 10^{21} carriers/cm^3. To ensure that the net Seebeck effect is large, there should only be a single type of a carrier. Mixed n-type and p-type conduction will lead to opposing Seebeck effect and low thermopower (defined here as absolute value of Seebeck coefficient).

By having a band gap large enough, n-type and p-type carriers can be separated, and doping will produce only a single carrier type. Thus good thermoelectric materials have band gaps large enough to have only a single carrier type but small enough to sufficiently high doping and high mobility (which leads to high electrical conductivity).

A good TE material also needs to have low thermal conductivity. Thermal conductivity in these materials arises from two sources of heat transport. Phonons traveling through the crystal lattice transport heat and lead to lattice thermal conductivity. The charge carriers (electrons or holes) also transport heat and lead to the electronic thermal conductivity. The electronic term is related to the electrical conductivity

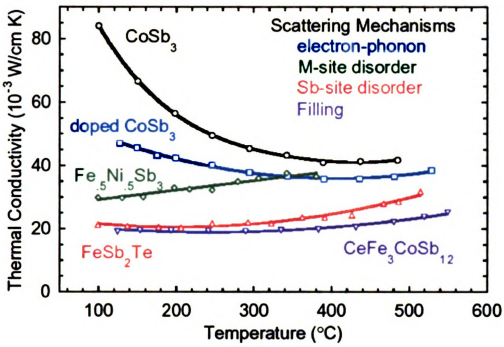

Figure 1.5: Thermal conductivity decreases in Skutterudites by the introduction of various scattering mechanisms. [reproduced with the permission of Dr. Jeff Snyder] [24]

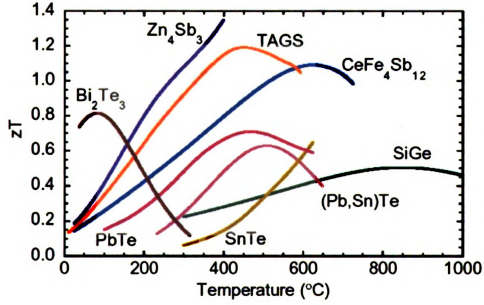

Figure 1.6: ZT for various p-type thermoelectric materials [reproduced with the permission of Dr. Jeff Snyder] [24]

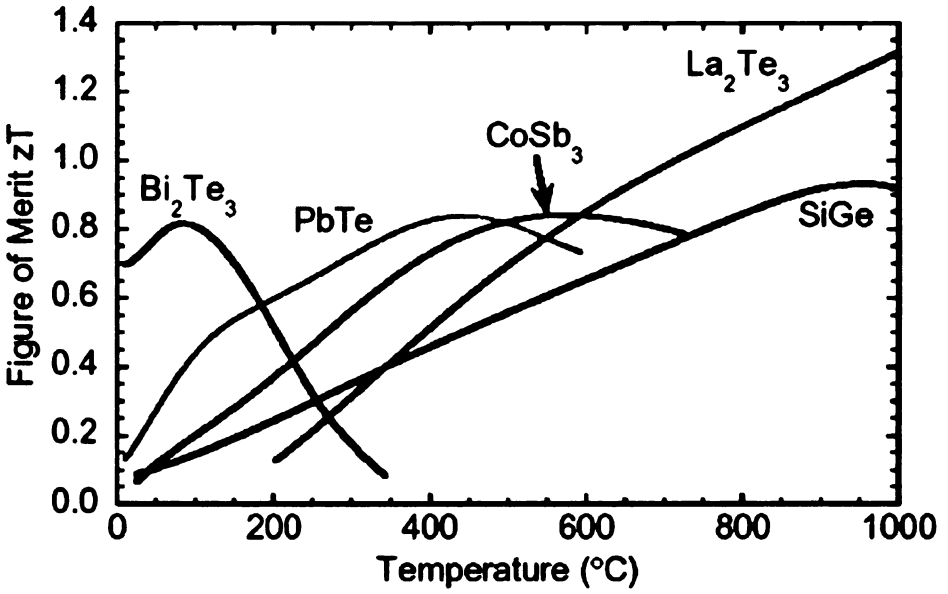

Figure 1.7: ZT for various n-type thermoelectric materials [reproduced with the permission of Dr. Jeff Snyder] [24]

through the Wiedeman$n$-Franz law

$$k_e = L\sigma\, T \tag{1.14}$$

where the Lorenz factor, L, depends slightly on the details of the band structure but for thermoelectric materials does not vary from the free electron gas value of

$$\frac{\pi^2 k_b^2}{3e^2} = 2.45 \times 10^{-8} V/K^2 \tag{1.15}$$

by more than a factor of 2.

Thus the greatest opportunity to enhance ZT is to minimize the lattice thermal conductivity. This can be achieved by increasing the phonon scattering by introducing heavy atoms, disorder, large unit cells, clusters and rattling atoms.

The ideal thermoelectric material is then one which is an "electron crystal - phonon glass" [7] where high mobility electrons are free to transport charge and heat but the

phonons are disrupted at the atomic scale from transporting heat [28].

Using these principles, a variety of high ZT materials have been developed. Many of these materials have an upper temperature limit of operation, above which the material is unstable. Thus no single material is the best for all temperature ranges, and different materials should therefore be selected for different applications based on the desired temperature range of operation. This leads to the use of a segmented thermoelectric generator.

ZT for various p-type and n-type thermoelectric materials are shown in Figures 1.6 and 1.7. Novel TE materials based around PbTe show great promise for operating temperatures at or slightly above the room temperature, and are therefore of particular interest. Recent advances have seen dramatic improvements in ZT by relatively small compositional changes, as illustrated in Figure 1.8 [29, 30, 31, 17]. These materials appear to exhibit nanoscale phase separation, or nanosize domains, as observed by high resolution imaging experiments, which could be an important structural ingredient necessary to enhance the TE figure of merit. However, the exact nature of these nanosize features (e.g. whether the inhomogeneities are bulk property of the samples or are just a surface effect) and their role for enhancement of the TE properties is not fully understood. This work represents a local structural study aimed to address some of these issues in this promising class of TE materials.

1.6 Thesis layout

This thesis is organized as follows. Next chapter provides a brief introduction into the atomic pair distribution function (PDF) technique and the rapid acquisition PDF experimental approach used in this study. Chapter 3 presents detailed local structural results on the high performance family of TE materials $AgPb_mSbTe_{m+2}$. This is followed by the results obtained for $Ag_{1-x}SnSb_{1+x}Te_3$ described in Chapter 4. Local structural perspective of the phase separation and TE properties in $(PbTe)_{1-x}(PbS)_x$

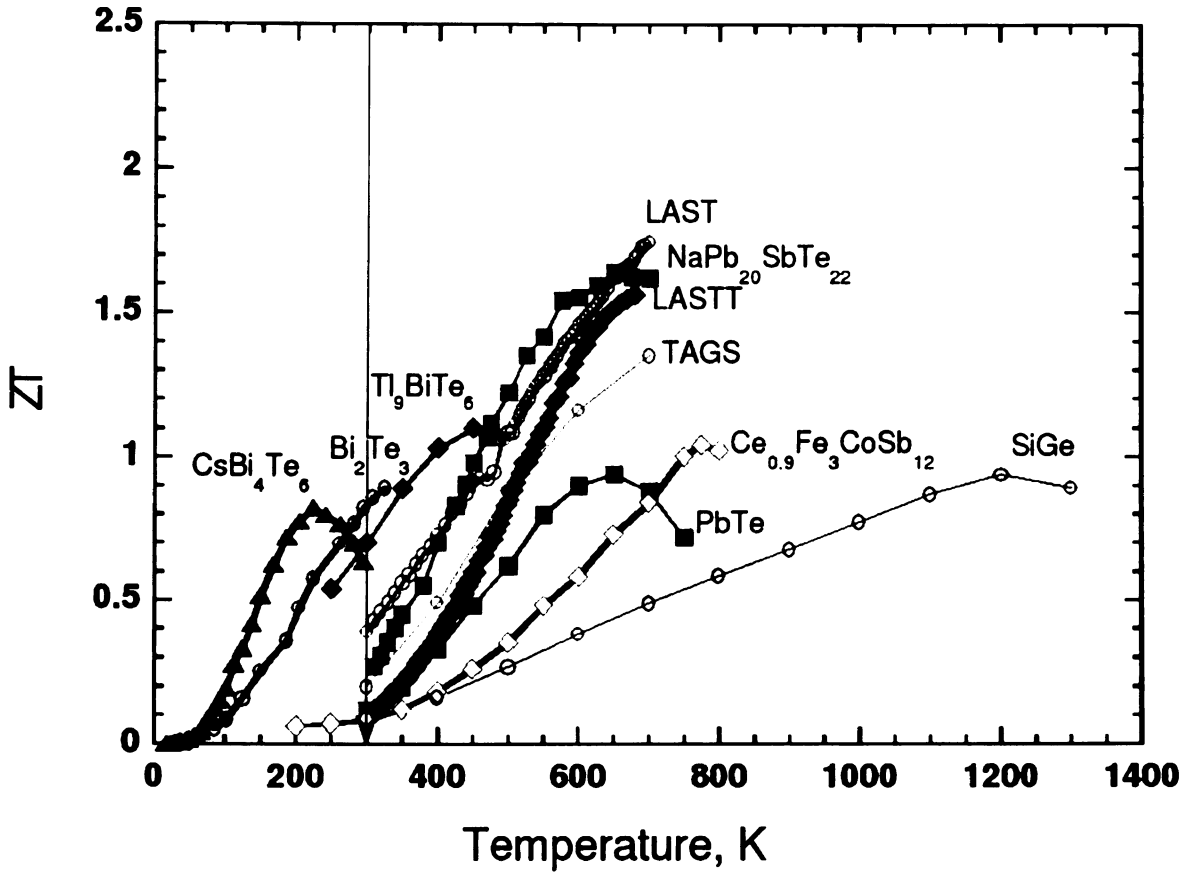

Figure 1.8: ZT for various PbTe based thermoelectric materials including recently discovered novel materials with dramatic ZT improvements compared to those shown in Figures 1.7 and 1.6. [reproduced with the permission of Prof. Kanatzidis]

are given in Chapter 5. Finally, in Chapter 6 concluding remarks are accompanied with comments on possible future research avenues for the local structural studies of this class of novel TE materials, which concludes the thesis.

Chapter 2

The Pair Distribution Function Method

2.1 Importance of the local structure

The structure plays an important role with regard to properties of modern materials. Advances in science and technology critically depend on our understanding and utilization of these properties. Many industrially important materials have complex structures which are usually difficult or impossible to study using conventional crystallographic method [32]. A significant fraction of the thermoelectric materials mentioned in Chapter 1 fall in this category. The structure of the three families of PbTe based thermoelectric materials investigated in this work and discussed in the following chapters can not be studied completely and accurately using conventional crystallography due to the limited structural coherence of the nanoscale features observed by imaging methods. Conventional crystallographic structural studies in such cases are often augmented by a local structural probe, such as extended x-ray absorption fine structure spectroscopy (EXAFS) [33], nuclear magnetic resonance (NMR) [34], or the atomic pair distribution function (PDF) technique [35].

The *local structure* plays an important role in many functional materials [35, 36].

It represents a description of the atomic neighborhood typically on a length-scale of several nanometers or shorter. Crystalline materials with well established *long range order* can be studied using conventional crystallography. In this case, the average structure obtained from conventional crystallography is the same as the local structure. However, structure of a large number of interesting functional materials does not possess long range periodicity. In such cases the real local structure usually deviates, sometimes quite dramatically, from the average structure obtained using conventional crystallographic methods. Understanding the underlying structure is important for understanding the material properties and for materials engineering.

Local structural probes such as NMR [34] and EXAFS [33] play an important role in revealing the local structure of a material. However, these methods can only detect local environments up to approximately 5 Å or less. To study the structures of complex materials on a length scale up to nanometers or even higher, different experimental methods need to be used, such as the atomic PDF method.

2.2 The atomic pair distribution function (PDF) technique

The atomic pair distribution function (PDF) technique is a total scattering based local structural method, that provides structural information on various length scales. Unlike crystallography (e.g. the Rietveld method) that uses structural information solely from the Bragg peaks, and disregards the rest of the diffraction pattern through a background function, total scattering methods use both Bragg peak and the diffuse scattering information. In this way both information about periodic structure and local deviations from periodicity are taken into account and treated on an equal footing. In recent years, the PDF method has demonstrated great power by being successfully used for solving various structural problems of wide range of functional

materials [35, 36] and gained appreciable attention from material science, solid state physics and chemistry communities.

2.2.1 History and current status of the PDF method

The PDF method was initially used to study structure of liquid and amorphous materials [37, 38, 39, 40]. In the past decade or so, it has been applied for the study of crystalline solids as well. The advent of synchrotron based radiation sources, such as pulsed spallation neutron sources and x-ray synchrotron sources, that provide high-intensity short-wavelength probes, has made the PDF method accurate and reliable. The PDF data analysis and modeling of crystalline materials are also highly computationally demanding and have become practical with the appearance of high-speed computers. In the past five years the PDF has also been utilized to study the structure of nanocrystalline materials [41], or materials with significant amount of disorder where nanometer scale plays an important role [42].

The PDF analysis applied to highly crystalline materials, such as Si or Ni, yields the structure in quantitative agreement with the average structure obtained through conventional crystallographic methods [43]. Complementary to the average structure analysis, Billinge *et al.* and Božin *et al.* have applied the PDF technique extensively to study the nature of the *local disorder* and nanometer scale inhomogeneities in otherwise well crystalline materials such as colossal magneto-resistive manganites and high temperature superconducting cuprates [44, 45, 46, 47, 48]. In cases when the long range crystallinity fades out gradually, such as in nano-crystalline and non-crystalline materials, the reciprocal space approach taken by the conventional crystallographic methods becomes less and less effective. The Bragg peaks become less and less sharp and there are fewer of them in the diffraction pattern which becomes rather featureless in such cases, making the conventional analysis rather hard if not impossible. However, this has little effect on the features obtainable through the

PDF technique where no long range periodicity is assumed. For example, Petkov *et al.* have shown that local and intermediate length-scale structures can be obtained from PDF data when a certain level of local atomic order is preserved [49, 50, 51, 52]. As for non-crystalline materials such as liquids, glasses, and amorphous materials, only the very local structure persists and the angstrom scale becomes the only meaningful length-scale. In such cases, the PDF technique represents the method of choice for structural investigations [53, 54, 55]. At present, with the advent of high flux instruments and with advancements in detector coverage, PDFs with significantly higher real space resolution have been achieved [56, 57, 58]. Complex modeling schemes, such as reverse Monte Carlo (RMC) and atomic pair potential based regression algorithms, are becoming popular tools in efforts for solving the structure of complex materials [59, 60, 61, 62, 63].

2.2.2 Definition of the PDF and its variants

The atomic pair distribution function (PDF), $G(r)$, is a one-dimensional pair correlation function that gives the probability of finding *atomic pairs* separated by a distance r. To obtain the PDF for a given structure, an atom i is selected, and its environment is inspected to look for its neighbors. A peak is assigned for every atom j found at the position corresponding to the inter-atomic distance r_{ij}, and zero everywhere else. Then the same procedure is repeated for all possible choices of atoms i, and the resulting functions are then averaged out to obtain the total $G(r)$ of the structure. In what follows, a series of definitions of various PDF variants is provided.

$$\rho(r) = \rho_0 g(r) = \frac{1}{4\pi N r^2} \sum_{\nu} \sum_{\mu} \delta(r - r_{\nu\mu}), \tag{2.1}$$

where ρ_0 is the number density in the system of N atoms. δ is a Dirac delta function. The function $\rho(r)$ is called the atomic pair density function (PDF). The function $g(r)$ is called the atomic pair distribution function, also abbreviated as PDF.

The PDF, g(r), is related to the radial distribution function (RDF), R(r), by $R(r) = 4\pi r^2 g(r)$. The radial distribution function has a useful property that the quantity $R(r)dr$ gives the number of atoms in an annulus of thickness dr at distance r from another atom. The coordination number, or the number of neighbors, N_C is then given by $N_c = \int_{r_1}^{r_2} R(r)dr$ where r_1 and r_2 are the lower and upper r-limits that define the RDF peak corresponding to the coordination shell in question.

Under the kinematic approximation, the sample scattering amplitude is,

$$\Psi(Q,t) = \frac{1}{\langle b \rangle} \sum_{\nu} b_\nu e^{iQR_\nu(t)} \tag{2.2}$$

where b_ν is the scattering amplitude of the atom ν, and $\langle b \rangle$ is the average value over all atoms. However, only the intensity of the diffracted beam, which is directly related to the square of the magnitude of $\Psi(\mathbf{Q})$, i.e. $|\Psi(\mathbf{Q})|^2$, can be measured. This is well known as the phase problem.

The coherent differential cross section is shown below:

$$\frac{d\sigma_c(\mathbf{Q})}{d\Omega} = \frac{\langle b \rangle^2}{N} |\Psi(Q)|^2 = \frac{1}{N} \sum_{\nu,\mu} b_\nu b_\mu e^{iQ(R_\nu - R_\mu)} \tag{2.3}$$

where N is the number of atoms in the whole sample.

Total scattering structure function is related to the measured intensity in the following way:

$$I(\mathbf{Q}) = \frac{d\sigma_c(\mathbf{Q})}{d\Omega} + \langle b \rangle^2 - \langle b^2 \rangle \tag{2.4}$$

and

$$S(\mathbf{Q}) = \frac{I(\mathbf{Q})}{\langle b \rangle^2} \tag{2.5}$$

Typically $S(\mathbf{Q})$ depends on both the amplitude and the direction of $\mathbf{Q}$. For samples of finely powdered crystallites, the scattering from the ensemble is isotropic. $S(Q)$ will then only depend on the magnitude of the wave vector $\mathbf{Q}$. This is known as powder averaging. The PDF can be directly obtained via a sine Fourier transform of S(Q):

$$G(r) = \frac{2}{\pi} \int_0^\infty Q[S(Q) - 1] \sin Qr dQ \tag{2.6}$$

On the other hand the following holds:

$$G(r) = 4\pi r \rho_0 (g(r) - 1) \tag{2.7}$$

$G(r)$ is usually called the reduced pair distribution function, while $g(r)$ is the pair distribution function. ρ_0 is the number density which is a constant for a specific structure, and represents number of atoms per unit cell volume.

As mentioned, the PDF analysis of powder diffraction data differs from the conventional crystallographic method in the way the diffuse scattering intensities in-between and underneath the Bragg peaks are treated. Conventional crystallographic analysis uses only the Bragg peaks which arise from the long range order of a structure. The PDF technique takes into account both the Bragg peaks and the diffuse scattering intensities which come from local deviations from the long range ordering. This is evident in the above equations. Therefore, the PDF method is capable of probing *both* the local and the average structure. This advantage over conventional analysis gives the PDF wider range of applicability. In the case of crystalline materials with disorder, the PDF technique and conventional crystallography are complementary, as the former provides additional information about the local structure. In the

case of nano-crystalline and non-crystalline materials, with few or no Bragg peaks, crystallography fails, and the PDF is the method of choice.

The PDF peaks in the low-r region contain the local structural information. Thus the real space resolution is an important factor when neighboring peaks are to be resolved. The atomic thermal motions broaden the PDF peaks. Termination effects due to finite measurement range give uncertainties in r value and also further broaden the peaks [64]. Therefore, to obtain high real space resolution it is usually required to obtain data over an extended Q range ($\geq$ 25.0 Å^{-1}), and to collect data at low temperature when possible. The PDF peak width and area reveal further details about the local distortions and number of neighboring atoms as well. The average structural information can be obtained from the PDF structural refinement using the least square regression fitting approach implemented in the program PDFFIT [65, 66]. The comparison between the calculated PDF based on the average structural model and the experimental PDF is a good way to check for the possible existence of local disorder. If the disorder is present, the average model is used as a starting point to build various potential models of the distorted structure, and these are then attempted to obtain a better fit.

Lattice vibrations can affect the PDF by modifying the Bragg peaks. This is described by the Debye-Waller factor. Real experimental measurements can only scan a finite region of Q-space. This introduces a cut-off in Q space, and thus induces fluctuations in the PDF signal. Background signal can also introduce fluctuations. The interested reader can look for quite detailed description of the technical issues of the PDF method in the literature. Excellent source is, for example, a book by Egami and Billinge [35].

2.3 Rapid acquisition PDF experiments and PDF data analysis

The PDF measurements using the conventional x-ray experimental setup involving goniometers and point detectors are typically very slow and usually take more than eight hours for collecting a dataset on a sample at a single temperature, even when using third generation synchrotron x-ray sources. This presented a bottleneck preventing the PDF technique from widespread application in areas such as nano-materials, for example, where only small quantities of specimens are available. Recent development of the rapid acquisition PDF (RA-PDF) method reduces the data collection time by three to four orders of magnitude [67]. This new approach in collecting data is briefly described below, followed by a brief description of program PDFgetX2 [68] used to obtain the PDF from raw x-ray powder diffraction data. The program PDFFIT2 will be introduced further as well, used to extract the structural information from the experimental PDFs.

2.3.1 Utilizing image plate detector for rapid data acquisition

The crucial part of the RA-PDF setup is the detection part. In RA-PDF experiment, an image plate (IP) detector is used, rather than a conventional solid state detector. This 2D data collection greatly reduces the data collection time, and opens new possibilities on the experimental front.

One layer of very small crystalline grains of photo-stimulable phosphor mixed with organic binders acts as a detecting medium. BaF(Br,I):Eu^{2+} is used as a photo-stimulable phosphor. This material is capable of storing a fraction of the absorbed x-ray energy, and emitting photo-stimulated luminescence (PSL) later when stimulated by visible laser light. The x-ray irradiation results in a certain number of Eu^{3+}

and F pairs proportional to the absorbed x-ray energy. The F centers are caused by the absence of halogen anions from their designated positions in the lattice. The energy trapping state of F centers is meta-stable with a long lifetime. However, the trapped electrons can be easily excited by visible light ($\geq$ 2 eV) to return to the conduction band. One of the processes occuring is the recombination of Eu^{3+} with one election to Eu^{2+}, along with the emission of a photon of 3.2 eV energy (blue light). A red He-Ne laser is usually used for the process of read-out. Its wavelength (632.8 nm) is considerably separated from the PSL wavelength (390nm). A conventional high-quantum efficiency photo-multiplier tube (PMT) is used to collect the photo-stimulated photons. The signal is then amplified and digitalized to be processed by computers. The remaining F centers in the phosphor after read-out can be further erased by exposing to visible light.

More technical details and extensive quantitative description on the characteristic of an IP detector can be found in [69, 70, 71, 72, 73, 74, 75, 76]. Dynamic range and linearity of the IP response, spatial resolution, active area size, and energy dependence are important technical issues for an IP as an x-ray area detectors. The standard procedure to get high quality data from RA-PDF experiment is described further.

2.3.2 The RA-PDF experimental procedure

The diffraction experiments for this study were performed at the 6ID-D beam line at the Advanced Photon Source (APS) located at Argonne National Laboratory, Argonne, IL (USA). High energy x-rays were delivered to the experimental hutch using a double bent Laue monochromator capable of providing a flux of 10^{12} photons/second and operating with x-rays in the energy range of 80-130 keV. Typical RA-PDF experimental setup is shown in figure 2.1.

A Mar345 image plate camera, a round disk with a diameter of 345 mm, was mounted orthogonal to the beam path, with the beam centered on the IP. The sample-

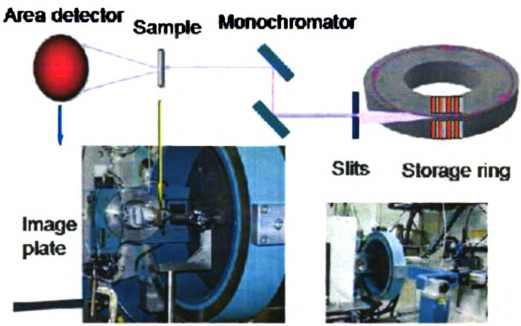

Figure 2.1: Experimental setup for the RA-PDF experiment. See text for details

to-detector distance can be determined by calibrating with a silicon standard sample [67] using the Fit2D program package [77].

Powder samples were carefully ground using a mortar and pestle and sieved to obtain fine powders. The powders were packed in a hollow flat aluminum plate sample container with cylindrical hole 5 mm in diameter, and sealed with kapton tape.

2.3.3 Data processing using FIT2D and PDFgetX2

All raw 2D data were integrated and converted to intensity versus 2θ format using the Fit2D program package [77], where 2θ is the angle between the incident and scattered x-rays. Figure 2.2 shows an example 2D diffraction pattern obtained from a Ni powder sample [67], used routinely in RAPDF experiments for calibration purpose. Multiple data sets for the same sample were combined using the same program. Data for the empty container were also collected and subtracted from the sample data during the correction step. Standard corrections for multiple scattering, polar-

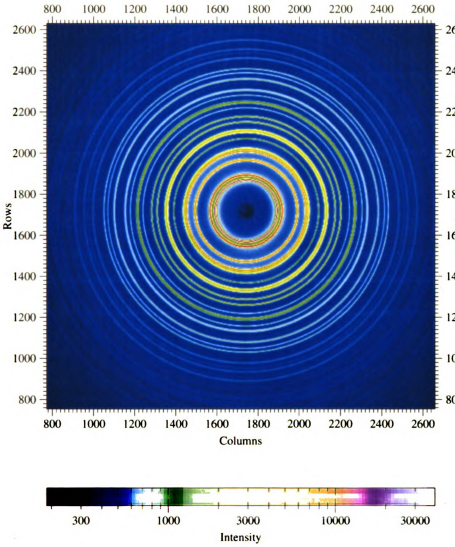

Figure 2.2: Two dimensional contour plot from the Mar345 Image Plate Detector. The XRD data are from nickel powder measured at ambient conditions. The wavelength of the radiation was 0.1270 Å. The concentric circles represent intersections of different scattering cones with the area detector (Debye-Scherrer rings). The sample was contained in a flat plate, 1.0 mm thickness, irradiated volume 0.25 mm^3, beam size 0.5× 0.5 mm^2. The small dark area in the center of the image is a shadow cast by the beam stop assembly [67].

ization, absorption, Compton scattering and Laue diffuse scattering were applied to the integrated data to obtain the reduced total structure function $F(Q)$, as described in detail in Refs. [67, 35]. Data correction and processing utilized the PDFgetX2 program package [68]. Figure 2.3 demonstrates the data processing path from $I(Q)$ to $G(r)$ for Ni powder data shown in Figure 2.2, as obtained from A. S. Masadeh.

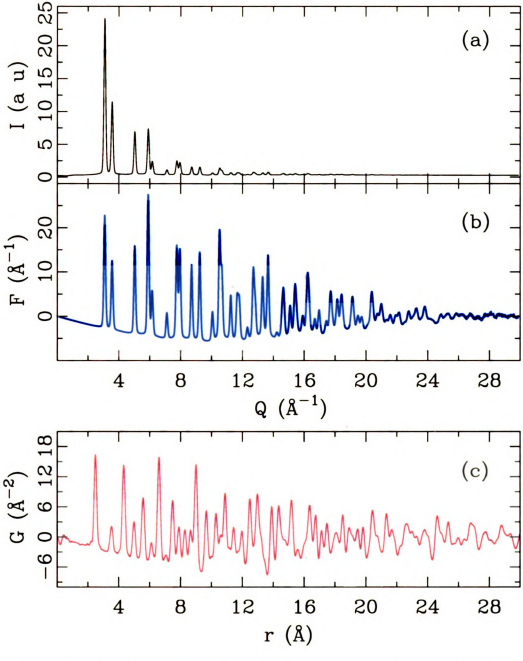

Figure 2.3: (a) The corrected experimental intensity of the Ni raw data shown in Figure 2.2, (b) the experimental reduced structure function $F(Q) = Q(S(Q) - 1)$ of data in (a), (c) the experimental $G(r)$ obtained by Fourier transforming the data in (b) with Q_{max} of 30.0 Å^{-1}. Credit: A. S. Masadeh.

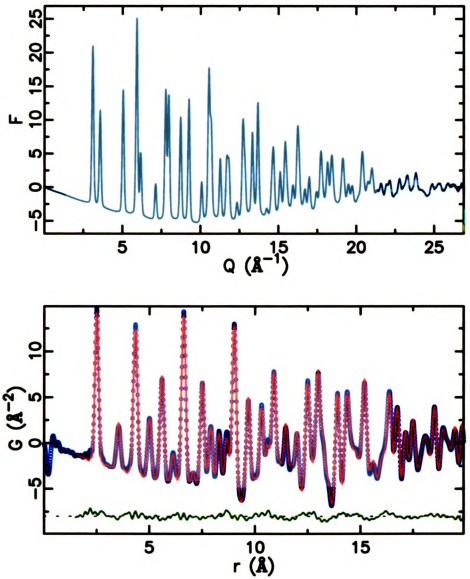

Figure 2.4: (top) Experimental F(Q) of Ni powder, and (bottom) experimental G(r) (symbols) with the fit of the structural model (solid line) and the difference curve underneath. Credit: H. J. Kim

PDFgetX2 is a GUI driven program used to obtain a pair distribution function from an x-ray powder diffraction data set. In the program PDFgetX2, a user-friendly graphical user interface (GUI) has been built to facilitate user interactions with data processing software. Standard corrections [35] such as various background subtractions, sample absorption, polarization, and Compton intensities are available. Oblique incident angle correction and empirical energy dependence of the detection efficiency are also implemented for RA-PDF setup. Standard uncertainties due to finite counting statistics are estimated and propagated in all steps. The $S(Q)$ data sets also contain the Faber-Ziman coefficients for all partial structure factors as additional columns. Example data processing is shown in Figure 2.3 as mentioned above.

2.3.4 Structural refinement using the PDFFIT program

Structural information was extracted from the PDFs using a full-profile real-space local-structure refinement method [43]. The program PDFFIT [65] has been used to fit the experimental PDFs, as well as an updated version of the program, PDFFIT2 [66], that is also available at the present time. An example fit, performed by H. J. Kim, is provided for the Ni powder data in Figure 2.4.

The PDFFIT program allows for multiple data-sets to be co-refined and is also capable of handling multiple phases. Starting from a given structure model and given a set of parameters to be refined, PDFFIT searches for the best structure that gives the best agreement between calculated PDF and the experimental PDF data. The residual function (Rw) is used to quantify the agreement of the calculated PDF from a model to the experimental data:

$$Rw = \sqrt{\frac{\sum_{i=1}^{N} \omega(r_i)[G_{obs}(r_i) - G_{calc}(r_i)]^2}{\sum_{i=1}^{N} \omega(r_i) G_{obs}^2(r_i)}} \tag{2.8}$$

The weight $\omega(r_i)$ is always set to unity in all the models attempted in this study.

2.3.5 Handling the multiphase problem

The ability to refine multiple phases in PDFFIT2 is an important feature extensively used in this study, since many of the samples used involve more than one phase. The detailed derivation of two-phase PDF is shown in the following series of equations. Generalization to the problems involving more than two phases can be obtained straight forwardly.

$$g(r) = \frac{1}{4\pi N r^2 \rho_0} \sum_i \sum_j [\frac{b_i b_j}{< b >^2} \delta(r - r_{ij})] \tag{2.9}$$

$$\begin{aligned} G'(r) &= \tfrac{1}{Nr} \textstyle\sum_i \sum_j [\frac{b_i b_j}{<b>^2} \delta(r - r_{ij})] \\ &= 4\pi r \rho_0 g(r) \end{aligned} \tag{2.10}$$

$$\begin{aligned} G(r) &= G'(r) - 4\pi r \rho_0 \\ &= \tfrac{1}{Nr} \textstyle\sum_i \sum_j [\frac{b_i b_j}{<b>^2} \delta(r - r_{ij})] - 4\pi r \rho_0 \\ &= \tfrac{1}{Nr} \textstyle\sum_m \sum_n [\frac{b_m b_n}{<b>^2} \delta(r - r_{mn})] + \tfrac{1}{Nr} \sum_p \sum_q [\frac{b_p b_q}{<b>^2} \delta(r - r_{pq})] - 4\pi r \rho_0 \\ &= \tfrac{<b_m>^2}{<b>^2} \tfrac{N_m}{N} \tfrac{1}{N_m r} \textstyle\sum_m \sum_n [\frac{b_m b_n}{<b_m>^2} \delta(r - r_{mn})] \\ &\quad + \tfrac{<b_p>^2}{<b>^2} \tfrac{N_p}{N} \tfrac{1}{N_p r} \textstyle\sum_p \sum_q [\frac{b_p b_q}{<b_p>^2} \delta(r - r_{pq})] - 4\pi r \rho_0 \\ &= \tfrac{<b_m>^2}{<b>^2} \tfrac{N_m}{N} g_m(r) + \tfrac{<b_p>^2}{<b>^2} \tfrac{N_p}{N} g_p(r) - 4\pi r \rho_0 \end{aligned} \tag{2.11}$$

$$N_m + N_p = N \tag{2.12}$$

$$G(r) = \frac{x_m < b_m >^2}{< b >^2} g_m(r) + \frac{x_p < b_p >^2}{< b >^2} g_p(r) - 4\pi r \frac{1}{x_m/\rho_m + x_p/\rho_p} \tag{2.13}$$

$$x_m = \frac{N_m}{N_m + N_p} \tag{2.14}$$

N_m, N_p are the numbers of atoms in each phase, N is the number of atoms in the whole system. $< b_m >$, $< b_p >$ is the average scattering power for each phase and $< b >$ is the one for the whole system. ρ_0 is the number density of atoms for the whole system, ρ_m and ρ_n are the number densities of atoms for each phase. Equation 2.14 shows important result that PDF contribution from each phase is weighted by the squared averaged scattering power from each phase multiplied by the number of atoms in each phase.

Chapter 3

Study of the structure of new thermoelectric material $AgPb_mSbTe_{m+2}$

3.1 Introduction

3.1.1 Background of $AgPb_mSbTe_{m+2}$ system

Pure PbTe is a narrow band n-type indirect bandgap semiconductors with the bandwidth of only 0.31 ev at room temperature. The highest ZT is 0.36 at 300 kelvin. With optimized doping, n-type doped PbTe can reach 0.84 at 648 kelvin while p-type can reach 0.7 at 698 kelvin.

Compounds in the series based on composition $AgPb_mSbTe_{m+2}$ can exhibit exceptional thermoelectric properties [17]. They are promising for electrical power generation and in the temperature range 600 to 900 kelvin, they are expected to significantly outperform all other reported bulk thermoelectric systems. The dimensionless thermoelectric figure of merit, ZT [78], of the $m \sim 18$ composition material was found to reach 1.7 at 700 kelvin, compared to the highest observed ZT of only 0.84 for PbTe

at 648 kelvin in n-doped material [79, 80]. This is a surprisingly large enhancement in ZT for the addition of just 10% per formula-unit of silver and antimony ions. It is clearly of the greatest importance to trace the origin of the ZT enhancement.

A recent theoretical analysis showed that resonant structures form in the DOS near E_f in the presence of ordered Ag and Sb atoms in the matrix and in the nanoclusters observed in HRTEM [81, 82]. The calculations used gradient corrected density functional theory and assumed different structural models for the clusters, since details of their structure and chemical ordering are not known. This type of DOS resembles that of the "best thermoelectric material" predicted earlier [82, 18].

3.2 Motivation

High resolution transmission electron microscopy (HRTEM) images from these materials indicate the presence of nanosized domains of a Ag-Sb-rich phase endotaxially embedded in the PbTe matrix [29]. An interesting possibility is that these nanoclusters are key components in the ZT enhancement. The HRTEM images show the clusters are randomly distributed through the matrix and are not long-range ordered. Randomly distributed nano-scale clusters which strain the lattice might be expected to increase phonon scattering and reduce the thermal conductivity which would enhance ZT provided the electrical conductivity was not degraded to a greater degree. An additional enhancement in ZT is possible if the material has an increased electronic density of states (DOS) at the Fermi-level, E_f.

The composition and atomic arrangements within the nanoclusters is a challenging topic since the clusters are not periodically long-range ordered. They are dispersed inside a matrix and cannot be studied crystallographically. A probing method sensitive to local structure is needed such as the atomic pair distribution function (PDF) analysis of x-ray powder diffraction data [35]. Detailed description on PDF method can be found in Chapter 2. Recently, the PDF was successfully used to study chemical

short-range ordered clusters randomly embedded in a parent matrix [83], in analogy with the present situation. Here we use PDF to study a series of compounds in the $AgPb_mSbTe_{m+2}$ series with $m = 6$, 12 and 18. For comparison we also studied the end member compound, PbTe, the $m = \infty$ member of the series. The resulting PDFs have sufficiently high quality to see a structural signature of the nanoclusters, even in the PbTe-rich $m = 18$ compound. These differences were sufficiently large to allow models of the local structure to be differentiated, confirming the existence of the clusters in the bulk, and narrowing down their composition and the atomic arrangement in the clusters.

3.3 Experimental details

3.3.1 Sample preparation

Ingots with nominal compositions $AgPb_6SbTe_8$, $AgPb_{12}SbTe_{14}$and $Ag_{0.86}Pb_{18}SbTe_{20}$ were synthesized by Eric Quarez in the laboratory of Prof. Mercouri Kanatzidis by annealing, in quartz tubes under vacuum, mixtures of Ag, Pb, Sb, and Te elements at 1000 °C for 8 h. This was followed by a fast cooling to 850 °C for 1 h, slow cooling to 800 °C for 12 h, and then cooling to 400 °C for 12 h. This method of cooling produces more consistent samples.

3.3.2 High energy x-ray diffraction experiments

X-ray diffraction measurements were made on the $AgPb_mSbTe_{m+2}$ series of materials with $m = 6$, 12, 18 and ∞ at room temperature using the recently developed rapid acquisition pair distribution function (RA-PDF) approach [67] at the MU-CAT 6-ID-D beam-line at the Advanced Photon Source (APS) at Argonne National Laboratory.

X-ray powder diffraction samples were prepared by carefully grinding the compounds in a mortar and pestle and sieving through a 400-mesh sieve. The pow-

ders were packed into hollow flat aluminum plate sample containers with a radius of 0.25 cm and thickness of 1.0 mm, sealed between thin Kapton films.

The x-ray energy used was 87.005 keV ($\lambda = 0.14248$ Å). The data were collected using a circular image plate (IP) camera Mar345, 345 mm in diameter. The camera was mounted orthogonally to the beam path with a sample-to-detector distance of 208.86 mm which was determined by calibrating with a silicon standard sample [67].

In order to avoid saturation of the detector, each measurement was carried out by multiple exposure to the x-rays. Each exposure lasted 10 seconds, and each sample was exposed five times to improve the counting statistics. An example of the raw data on the image plate is shown in Figure 3.1(a).

All raw 2D data were integrated and converted to intensity versus 2θ format using the Fit2D program package [77], where 2θ is the angle between the incident and scattered x-rays. Data sets for the same sample were combined using the same program. Data for the empty container were also collected and subtracted from the sample data during the correction step. Standard corrections for multiple scattering, polarization, absorption, Compton scattering and Laue diffuse scattering were applied to the integrated data to obtain the reduced total structure function $F(Q)$, as described in detail in Data correction and processing utilized the PDFgetX2 program package [68]. An example of the $F(Q)$ for the $m = 18$ sample is shown in Figure 3.1. Sine Fourier transformation of $F(Q)$ gives the atomic PDF, $G(r)$, according to $G(r) = \frac{2}{\pi}\int_{Q_{min}}^{Q_{max}} F(Q)\sin(Qr)\,dQ$, where Q is the magnitude of the scattering vector. The good statistics in the high-Q region of the data (Figure 3.1(b)) allowed a $Q_{max} = 26.5$ Å^{-1} to be used which gives high-quality PDFs with good resolution. This is evident in Figure 3.1(c) where $G(r)$ is plotted for the sample $Ag_{0.86}Pb_{18}SbTe_{20}$.

The $G(r)$ data for all samples are plotted in Figure 3.2 on top of each other. The difference curves plotted below are the differences between the different m-value PDFs and pure PbTe. The difference curves show fluctuations that are much larger than

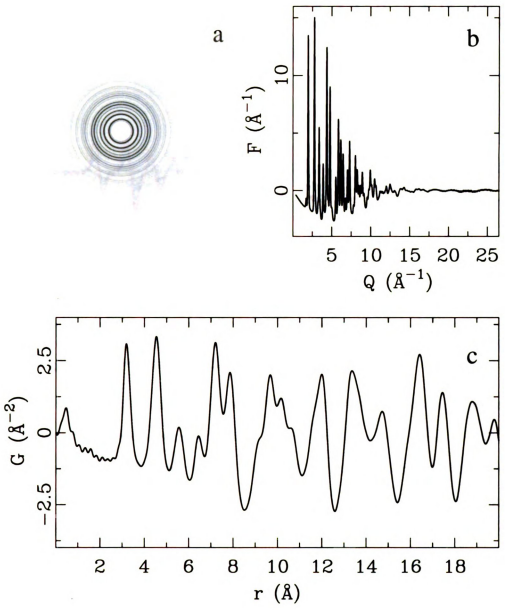

Figure 3.1: (a) The raw data diffraction pattern observed on the image plate. (b) $F(Q)$ and (c) $G(r)$ for the $Ag_{0.86}Pb_{18}SbTe_{20}$ sample. In the Fourier transform, Q_{max} was set to 26.5 Å^{-1}.

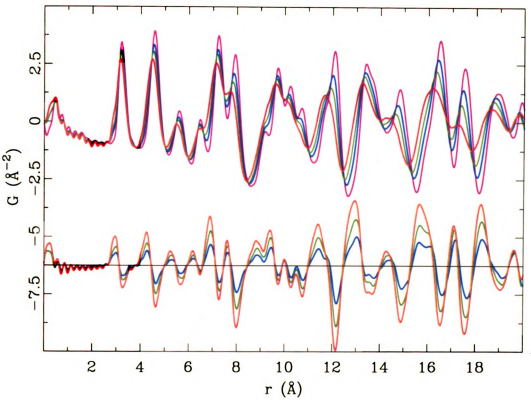

Figure 3.2: $G(r)$ and $DG(r)$ (compared to PbTe) for samples with different m value. Magenta curve is for PbTe, blue curves are for sample $Ag_{0.86}Pb_{18}SbTe_{20}$, green for sample $AgPb_{12}SbTe_{14}$, red for $AgPb_6SbTe_8$.

the estimated random errors on the data and therefore have a real origin, encoding the local structural differences between the $AgPb_mSbTe_{m+2}$ and PbTe compounds. The fluctuations in the difference curves are highly correlated between the different m-values, growing in amplitude from $m = 18$, 12 to 6, as expected. This suggests that the local structures in each case are similar and gives some confidence that the results from lower m-value compounds can give insight about higher m-members. It also gives us confidence that the smaller ripples in the difference curve from the $m = 18$ compound have a real structural origin. $m = 12$ and 2.5 to compare with $m = 6$ are shown also.

3.3.3 Modeling

Structural information was extracted from the PDFs using a full-profile real-space local-structure refinement method [43] analogous to Rietveld refinement [32]. We used an updated version[84] of the program PDFFIT [65] to fit the experimental PDFs. PDFFIT allows for multiple data-sets to be refined and can also handle multiple phases. Starting from a given structure model and given a set of parameters to be refined, PDFFIT searches for the best structure that is consistent with the experimental PDF data. The residual function (Rw) is used to quantify the agreement of the calculated PDF from model to experimental data:

$$Rw = \sqrt{\frac{\sum_{i=1}^{N} \omega(r_i)[G_{obs}(r_i) - G_{calc}(r_i)]^2}{\sum_{i=1}^{N} \omega(r_i) G_{obs}^2(r_i)}} \tag{3.1}$$

Here the weight $\omega(r_i)$ is set to unity.

In this modeling we took advantage of the ability to refine multiple phases in PDFFIT. We searched for domains of Ag and Sb rich material embedded in the PbTe matrix. Provided we fit the PDF over a range of r that is much less than the particle diameter, it is a good approximation to model the data as being made up of two distinct phases. This neglects cross-terms; i.e., atom pairs where one atom is in one phase and the neighboring atom is in the other phase. However, our experience suggests that these terms are small and a reasonable and simple starting point is to neglect these terms and model the phases as distinct (i.e., incoherent). The HRTEM images suggest that the nano-cluster domains have diameters of the order of a few nanometers and our fitting is carried out over a range up to 20 Å. Thus, some inconsistencies in the fits in the high-r range should be attributable to the neglected cross-terms. This approximation can be removed in the future, but only at the expense of having to fit the data with very large models. The success of the current modeling seems to suggest that this is not warranted at this point.

In PDFFIT, each phase in the multi-phase mixture has its own scale-factor that is refined. This scale factor reflects both the relative phase-fraction of the phases, but also any differences in the scattering power of the two phases, which depends on the respective compositions of the phases. In Chapter 2, we derived the mathematical equation defining PDF in multiphase. Here we present the equations that allow us to extract phase fractions from the refined scale factors of the phases. In PDFFIT, the total PDF $G(r)$ is defined as a summation of the different phases as follows:

$$G'_s(r_k) = f_s B_s(r_k) \Sigma_{p=1}^{P} f_p G_p^s(r_k), \tag{3.2}$$

where f_s is the overall scale factor and B_s is an experimental resolution factor for data set s. The sum is over the different structural phases, p, in a multiphase refinement and $G_p(r_k, s)$ is the model PDF for a single phase p. The weighted abundance of each phase is given by $f_p = \frac{<b_p>^2}{<b>^2} \frac{N_p}{N}$ where $\langle b_p \rangle$ and $\langle b \rangle$ are the averaged scattering factors for phase p and the whole sample, respectively, and N_p and N are the total atom number for phase p and the whole sample. We can easily calculate $\frac{N_p}{N}$ from the stoichiometry of phase p and the whole sample. After refinement we extract $\frac{N_p}{N}$ from the weighted scale factor and then compare it to the calculated one to see whether the refinement result is self-consistent with the known stoichiometry. For example, let's suppose we use two phases PbTe and $AgPb_xSbTe_{x+2}$ to model $AgPb_mSbTe_{m+2}$. We can set up the following two equations to get $\frac{N_{PbTe}}{N}$ and $\frac{N_x}{N}$:

$$\frac{N_x}{2x+4} = \frac{xN_x}{m(2x+4)} + \frac{N_{PbTe}}{2m}, \tag{3.3}$$

and

$$N_x + N_{PbTe} = N. \tag{3.4}$$

Since x and m are known we can extract the expected ratio $\frac{N_p}{N}$ for comparison with

the value obtained from the refinement.

To test this procedure, we used a sample made by mechanically mixing PbTe and $AgSbTe_2$ powders with atom number ratio of 1:3 and carried out a two-phase refinement. The refined value of $\frac{N_p}{N}$ was 0.69 compared to the expected values of 0.75. This suggests that we can obtain the phase fractions to an accuracy at the 10% level.

Each data-set (for the finite-m cases) was modeled with a sequence of models. Model H is a single phase homogeneous model of the correct average composition. Models $NC0_n$, $NC1_n$, $NC2_n$, $NC3_n$ and $NC4_n$ are two-phase models that test for the presence and nature of nanoscale clusters in the material ('NC' refers to nano-cluster). In all the NC models, the first phase is always a pure PbTe component. The second phase comes from the embedded nanoclusters where we have tried different models varying their composition and chemical ordering. The number after the NC, '0', '1', '2', '3' or '4', refers to the increasing Pb component in the second phase as will be explained in more detail later. The integer index n refers to a different chemically ordered variant of each nanocluster model, where n increases when the chemical ordering in the special variant increases.

In solid solution model H, one homogeneous phase is defined in which the dopant Ag, Sb atoms randomly occupy the Pb sublattice. The cubic symmetry of the PbTe matrix is retained, and thus only one lattice parameter is refined. These models have four refinable structural parameters and two experimental parameters for a total of six refinable parameters. The PbTe structure is shown in Figure 3.3(a).

In the case of $NC0_n$, a two-phase model is applied. The major phase is still PbTe. The chemical component of the second phase is the same as bulk $AgSbTe_2$ [85]. In this model there are no Pb atoms inside the minor phase. For the minor phase of this model we tried both a chemically disordered cluster model $NC0_0$ with a cubic unit cell and Ag, Sb atoms distributed randomly on the lead sublattice (Figure 3.3(b)) and a tetragonal unit cell with Ag and Sb atoms chemically ordered on the Pb

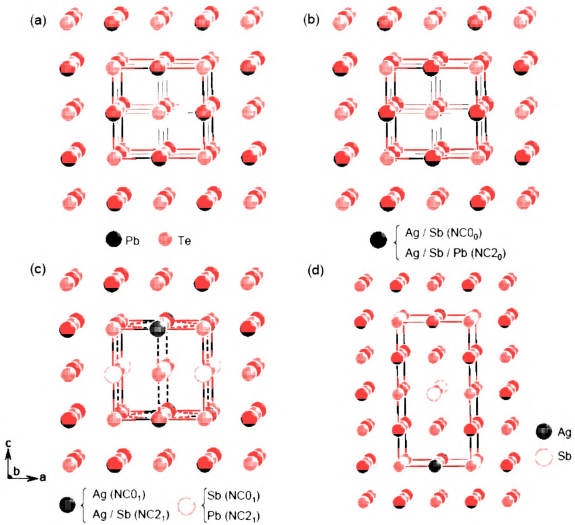

Figure 3.3: The unit cells for different models are shown here. (a) is the PbTe major phase. In all plots Te is shown as red atoms and Pb as green. (b) Chemically disordered $AgSbTe_2$ in $NC0_1$ and chemically disordered $AgPb_2SbTe_4$ in $NC2_0$. (c) Chemically ordered $AgSbTe_2$ in $NC0_1$ and partially chemically disordered $AgPb_2SbTe_4$ in $NC2_1$. (d) Chemically ordered $AgPb_2SbTe_4$ in model $NC2_2$ resulting in 2-fold supercell along one crystal axis. In all models the Te (red) sublattice is not changed.

sublattice sites ($NC0_1$, Figure 3.3(c)). These models have nine and eleven structural parameters, respectively, resulting in eleven and thirteen total refinable parameters.

The model $NC2_n$ also contains two phases, the major phase is still PbTe while the minor phase contains atoms with the chemical composition of $AgPb_2SbTe_4$. In this model, we also tried various possible chemical ordering possibilities for the minor phases, which can be totally chemically ordered ($NC2_2$), partially chemically ordered ($NC2_1$) and totally chemically disordered ($NC2_0$). In the totally chemically ordered case, the unit cell contains 16 atoms forming 4 layers as shown in Figure 3.3(d). There are two types of layer. Ag, Sb and Te atoms form one type of layer and Pb, Te atoms form the second type. The two types of layer intersect with each other. The two lattice parameters in the plane of the layer are the same, but the lattice parameter in the perpendicular direction is approximately doubled. The resulting symmetry is refined as tetragonal. This model has twelve structural parameters and fourteen total refinable parameters. In the $NC2_1$ variant, Ag and Sb atoms distribute randomly in their plane but do not substitute on the Pb or Te sites (Figure 3.3(c)). In the $NC2_0$ case, (Figure 3.3(b)) Pb, Sb and Ag atoms distribute randomly on the metal sublattice of the whole minor phase resulting in a cubic structure. In both of the two latter cases, there are only eight atoms in the unit cell. These models have eleven and nine structural, and thirteen and eleven total refinable parameters, respectively.

Models $NC1_0$, $NC3_0$ and $NC4_0$ are almost the same as model $NC2_0$ except that the chemical compositions of the minor phase are $AgPbSbTe_3$, $AgPb_3SbTe_5$ and $AgPb_4SbTe_6$, respectively. The modeling of the different $NC2_n$ models indicated that the PDF was not sensitive to the degree of chemical ordering in the minor phase and the results for chemically ordered or partially ordered cases of models $NC1_n$, $NC3_n$ and $NC4_n$ are not presented here.

All refinements were performed over the range of PDF from 2.85 Å to 20 Å. The PbTe end member compound was fit with a homogeneous model H and two-phase

models $NC1_n$ and $NC2_n$. All models were fit to the $m = 6$, 12 and 18 datasets.

3.4 Results

First we consider the pure PbTe end-member compound. The homogeneous model H, as expected, fit reasonably well resulting in an $Rw = 0.086$. Displacement parameters, U_{iso}, for Te and Pb atoms are 0.013 Å^2 and 0.029 Å^2 respectively and the lattice parameter is 6.47 Å. Refining the two-phase model $NC0_n$ and $NC2_n$ to the PbTe data did not result in an improvement in Rw despite the greater number of parameters. The scale factor for the second, non-physical, phase becomes very small (smaller than 0.3 percent), and the displacement parameters in this phase also become very large, indicating that the fit is attempting to eliminate the second phase. The result from the two phase refinement shows that the PDF is able to distinguish single from two-phase behavior.

We now turn our attention to the $m = 6$ compound that has the largest volume fraction of second phase in it. First this was fit with the homogeneous model H. The fit is poor as shown in Figure 3.4(a), with $Rw = 0.212$.

Significantly better fits were obtained from the two-phase models (Table 3.1, Table 3.2 and Figure 3.4(b)) with $Rw = 0.0724$ from the chemically disordered model $NC2_0$. The refined values are shown in Table 3.1 and Table 3.2. Similar results were obtained from the chemically disordered models. This analysis strongly suggests that the Ag and Sb clusters are present in the bulk of the material and are not an artifact of the TEM measurement.

We now wish to differentiate between the different composition two-phase models $NC0_n$–$NC4_n$. In terms of fit to the data and Rw, all four models performed comparably well, both in the chemically ordered and disordered states. The refined parameters that produce these good fits allow us to differentiate somewhat between the models. In particular, the refined phase fractions for the two phase refinements

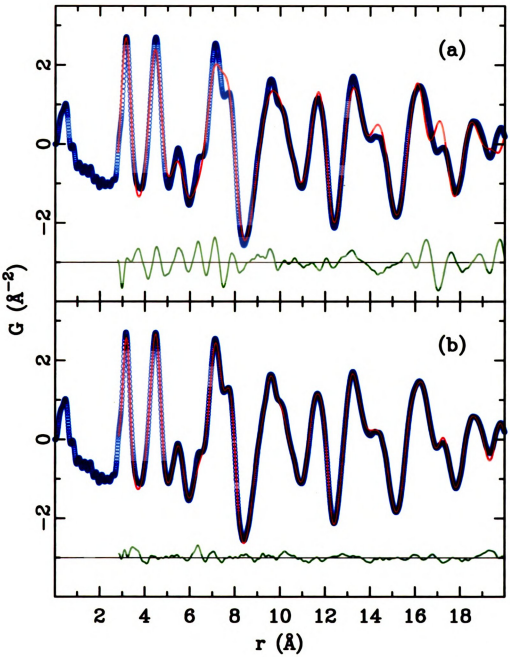

Figure 3.4: (a) PDF from the homogeneous H model for sample $AgPb_6SbTe_8$. The line with empty circles is the data, the solid line is the calculated curve from the fitting and the line offset below is their difference. (b) Chemically disordered case of model $NC2_0$ for $AgPb_6SbTe_8$. Line attributions are the same as in (a).

Table 3.1: Results from PDFFIT for the $AgPb_6SbTe_8$ sample. $n = \frac{N_{PbTe}}{N}$ is the ratio of atom numbers in PbTe phase to whole sample, n_0 is the expected ratio calculated from the chemical stoichiometry (see text for details). U_{atom} are the displacement parameters for atoms on different sites.

		model H	$NC0_0$	$NC0_1$	$NC1_0$
PbTe	R_w	0.22	0.066	0.065	0.070
	n/n_0	-	0.276/0.750	0.257/0.75	0.321/0.625
	a	-	6.41	6.41	6.41
	U_{Te}	-	0.0291	0.0255	0.0299
	U_{Pb}		0.0295	0.0307	0.0297
Phase 2	a	6.33	6.22	6.21	6.22
	c	-	-	6.24	-
	U_{Te}	0.080	0.0480	0.0488	0.0415
	U_{Pb}	0.061	-	-	0.08444
	U_{Ag}	0.061	0.0782	0.0382	0.0844
	U_{Sb}	0.061	0.0782	0.203	0.0844

Table 3.2: Results from PDFFIT for the $AgPb_6SbTe_8$ sample. $n = \frac{N_{PbTe}}{N}$ is the ratio of atom numbers in PbTe phase to whole sample, n_0 is the expected ratio calculated from the chemical stoichiometry (see text for details). U_{atom} are the displacement parameters for atoms on different sites.

		$NC2_0$	$NC2_1$	$NC2_2$	$NC3_0$	$NC4_0$
PbTe	R_w	0.072	0.070	0.075	0.070	0.071
	n/n_0	0.358/0.500	0.383/0.500	0.372/0.500	0.376/0.325	0.404/0.250
	a	6.41	6.41	6.41	6.41	6.41
	U_{Te}	0.0285	0.0305	0.0297	0.0299	0.0299
	U_{Pb}	0.0320	0.0298	0.0311	0.0294	0.0293
Phase 2	a	6.22	6.23	6.226	6.219	6.220
	c	-	6.19	12.40	-	-
	U_{Te}	0.0704	0.0409	0.0325	0.0384	0.0377
	U_{Pb}	0.0550	0.0852	0.0875	0.08724	0.0879
	U_{Ag}	0.0550	0.0852	0.0875	0.08724	0.0879
	U_{Sb}	0.0550	0.0852	0.0875	0.0872	0.0879

can be compared with the values that should be obtained based on the overall chemical composition of the material. As can be seen in Table 3.1 and Table 3.2, the $NC0_n$ and $NC1_n$ models significantly underestimate, and $NC4_n$ significantly overestimates, the phase fraction. The $NC2_n$ and $NC3_n$ compositions give phase fractions much closer to those stoichiometrically expected, with $NC3_n$ giving the best agreement. This is strong evidence that the nanoclusters contain significant amounts of Pb atoms and are not pure $AgPb_6SbTe_8$.

The refinements suggest that the average composition of the nanoclusters is "$AgPb_3SbTe_5$". However, it is unlikely that the real clusters have this composition since it is not possible to construct an ordered model with this composition by interleaving Ag/Sb and Pb layers on the Pb sublattice; it is necessary to have a layer with Ag/Sb mixed with Pb. As we discuss below, this is not expected on theoretical grounds. It could come about due to the presence of anti-phase boundaries between Pb regions and Ag/Sb regions, in analogy with the Na_3BiO_4 material studied previously [83], though it seems unlikely that this can occur within an individual nanocluster. From this point of view, it seems more likely that clusters with compositions of $AgPb_2SbTe_4$ and $AgPb_4SbTe_6$ coexist in the matrix yielding, on average, the observed "$AgPb_3SbTe_5$" composition. It should also be noted that some uncertainty exists in the two-phase modeling, especially taking into account the fact that we are modeling coherently embedded nanoclusters approximated as an incoherent mixture. The strong result is that significant Pb content exists in the nanoclusters but there is probably some uncertainty on the precise value.

We investigated the chemical ordering within the nanoclusters by focusing on the $NC2_n$ model that lends itself to rational chemically ordered models. Refinements of the chemically disordered and partially ordered variants of models $NC2_n$ yielded comparable fits to the chemically ordered fits, with comparable values of refined parameters (Table 3.1 and Table 3.2) suggesting that the current PDF measurements

Table 3.3: Results from model $NC3_0$ for three different m-members. $n = \frac{N_{PbTe}}{N}$ is the ratio of atom numbers in the PbTe phase to whole sample, n_0 is the expected ratio calculated from chemical stoichiometry. U_{atom} is the thermal factor for atoms on different site.

		$AgPb_6SbTe_8$	$AgPb_{12}SbTe_{14}$	$Ag_{0.86}Pb_{18}SbTe_{20}$	PbTe
PbTe	R_w	0.072	0.066	0.074	0.086
	n/n_0	0.376/0.325	0.571/0.643	0.693/0.750	-
	a	6.41	6.43	6.45	6.47
	U_{Te}	0.029	0.0246	0.0214	0.013
	U_{Pb}	0.032	0.0280	0.0262	0.029
Phase 2	a	6.22	6.26	6.29	-
	U_{Te}	0.0371	0.0779	0.0826	-
	U_{Pb}	0.0815	0.0876	0.0691	-
	U_{Ag}	0.0815	0.0876	0.0691	-
	U_{Sb}	0.0815	0.0876	0.0691	-

alone are not sensitive enough to differentiate the chemical ordering within the minor phase.

Finally, we note that similar results were obtained when the $m = 12$ and $m = 18$ samples were refined in the same way. The results for the chemically disordered "$AgPb_3SbTe_5$" model are presented in Table 3.3. The refined phase fractions nicely track the nominal composition giving us good confidence that the two-phase modeling is giving physically meaningful results and that nanoclusters of average composition close to $AgPb_3SbTe_5$ are present.

3.5 Discussion

The success of models $NC2_n$ and $NC3_n$ verify that the TEM observations of nanoclusters reflect a bulk average property of this material. These models also provide evidence for the chemical composition of the minor phase and give a hint to the chemical distribution of Ag, Sb and Pb atoms in the minor phase, although little information is available about the degree of chemical ordering.

In Figure 3.5 we show a HRTEM image that suggests that clusters are present

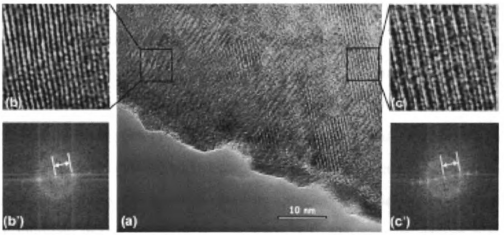

Figure 3.5: A HRTEM image of a region of a sample of $Ag_{0.86}Pb_{18}SbTe_{20}$. The four smaller pictures at the side are the amplified pictures for different (lattice) local region and their fourier transformed images [1]

that result in a doubling of the lattice parameter in the second phase, though not all clusters show this behavior. This is consistent with the partially or fully ordered model $NC2_n$ variants, $n = 1, 2$, which alternate Pb and Ag/Sb layers on the metallic sublattice. The fully chemically ordered case in model $NC2_2$ was found to be the stable configuration in a coulomb lattice-gas Monte Carlo simulation study of the ground state of this system as a function of m [86]. Thus, we believe that clusters with the totally chemically ordered form in model $NC2_2$ (Figure 3.3(d)) are present as nanoclusters in the large m compounds. This may not be the unique form of the nanoclusters, and indeed, not all the nanoclusters evident in the TEM images show this cell doubling. They presumably form by a nano-phase separation of constituents accompanied by an imperfect and defective ordering and there appears to be considerable spatial disorder of the chemical constituents; though the nanoclusters are coherently endotaxially embedded in the matrix, they are not well ordered. Incorporating more Pb in the nanoclusters allows the system to balance its desire to phase separate, with maintaining a degree of lattice matching to keep the nanoparticles embedded in the matrix without incoherent interfaces. The refined lattice parameters for the nanocluster phases are smaller than the matrix: 6.23-6.29 Å compared

to 6.41 Å for the strained matrix and 6.47 Å for relaxed PbTe. Both the chemical inhomogeneities and the inhomogeneous lattice strain are likely to increase phonon scattering. The size of the nanoclusters may also be important in making this scattering mechanism effective. It was claimed in [81] that the short-range nature of the local chemical ordering can broaden out Fermi-surface resonances which plays an important role in thermopower enhancement. More recent theoretical calculations on electronic conductivity and Seebeck coefficient suggest that the power factor is only slightly modified in the $AgPb_mSbTe_{m+2}$system [87]. The main reason for observing enhanced ZT in this system comes from a reduction of the lattice thermoconductivity due to the presence of nanoclusters [88, 87]. This is consistent with people's intuition on such system and also our result. Presumably, the size of the nanoclusters, their exact composition, the atomic ordering within them and their concentration with PbTe will be a sensitive function of the preparation conditions.

Adding Pb atoms in the minor phase greatly improves the result of the refinement. The reason is that Pb atomic number is much larger than the atomic numbers of Ag, Sb and Te and its scattering factor is quite different from those of the other three.

3.6 Summary

In this structural study based on the PDF method, we verified that in the bulk material of $AgPb_mSbTe_{m+2}$, nanoclusters of a minor phase containing Ag, Pb, Sb and Te atoms form in the matrix of PbTe. We give evidence showing that the chemical composition of the minor phase is most likely between $AgPb_2SbTe_4$ and $AgPb_4SbTe_6$. We propose a structure for the minor phase based on PDF, TEM and theoretical considerations.

Chapter 4

Thermoelectric material $Ag_{1-x}SnSb_{1+x}Te_3$

4.1 Interesting physics in the $Ag_{1-x}SnSb_{1+x}Te_3$ system

Theoretically there is no upper limit for ZT but, physically, electron conductance σ, Seebeck coefficient S and thermal conductance κ depend on each other. This is why it is difficult to find high ZT materials. Traditionally, heavily doped ($\sim 10^{19}$ carriers/cm^3) semiconductors provide the best compromise in getting high ZT [2]. All materials used in current thermoelectric devices are heavily doped semiconductors.

When the doping exceeds 10^{20} carriers/cm^3, it generally leads to a very small Seebeck coefficient, $S < 60\mu V/K$ [30]. $Ag_{0.85}SnSb_{1.15}Te_3$ is unusual in that it shows an almost metallic carrier concentration($\sim 5 \times 10^{21}$cm^{-3}) but also possess a large Seebeck coefficient of the order of $\sim 160\mu V/K$ at $600K$ [30]. $Ag_{0.85}SnSb_{1.15}Te_3$ is a non-stoichiometric derivative of $AgSnSbTe_3$, which is formed from the combination of two narrow band-gap semiconductors, $AgSbTe_2$ and Sn_4Te_4, both of which adopt the rock salt (NaCl) structure. $Ag_{0.85}SnSb_{1.15}Te_3$ exhibits a large thermoelectric

power response. The carriers are holes that have an anomalously heavy mass and exhibit other anomalous properties such as a quadratic temperature dependence of the resistivity over a very wide range of T [30]. There are many poorly understood aspects of this material and its high ZT, not least the fact that it is p-type, rather than an n-type semiconductor at all [30].

As with the other thermoelectric materials studied in this thesis work, HRTEM indicates that $Ag_{0.85}SnSb_{1.15}Te_3$ is a nano-structured composite rather than a solid solution [30] as seen in Figure 4.1. This nano-structure is evident throughout the crystal and the material is thought of as a type of bulk nano-composite [30]. The nano-regions have a structure that is significantly modified from the matrix (Figure 4.1(b)) and coherently embedded (Figure 4.1(c)). These compositional fluctuations at the nanoscopic level are similar to those of $AgPb_mSbTe_{m+2}$ system (as described in Chapter 3).

4.2 PDF study of the $Ag_{1-x}SnSb_{1+x}Te_3$ system

4.2.1 Introduction

The composition and atomic arrangements within the nanoclusters is a challenging topic since the clusters are not periodically long-range ordered, but dispersed inside a matrix, and cannot be studied crystallography. A method sensitive to local structure is needed such as the atomic pair distribution function (PDF) analysis of X-ray powder diffraction data [35]. As discussed in chapter 3, this approach was successfully used to study chemical short-range ordered clusters randomly embedded in a parent matrix [1, 83], in analogy with the present situation. Here we report a PDF study of the compounds $Ag_{1-x}SnSb_{1+x}Te_3$. For comparison we also studied the end member compounds, $AgSbTe_2$, and $AgSn_2SbTe_4$.

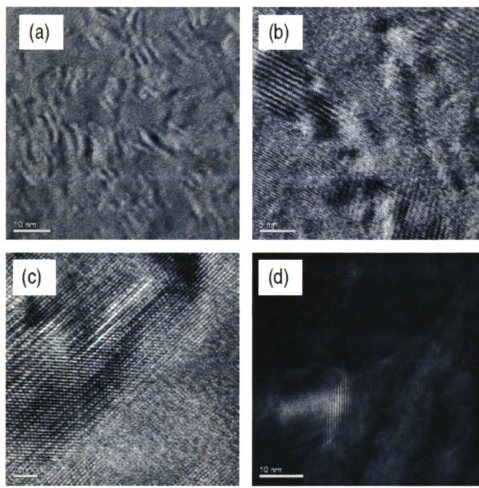

Figure 4.1: (a) High resolution TEM image of $Ag_{0.85}SnSb_{1.15}Te_3$ that shows a nano-structured region of the crystal. The nano-structures have geometrical dimensions of 3 - 30 nm and are dispersed throughout the crystal evenly. (b) A close-up view of an embedded nanocrystal. (c) The interface region between the embedded nanocrystal and the matrix showing a high degree of coherency. (d) Dark field imaging over a limited area in the crystal that shows the compositional variations between the matrix and the embedded nanocrystal. (Scales for (a) 10 nanometers, (b) 5 nm, (c) 20 nm, (d) 10 nm) [reproduced from [89] with permission from M. G. Kanatzidis]

4.2.2 Experimental Details

Sample Preparation

Sn_4Te_4 and $AgSbTe_2$ are the natural end-member compositions for the $Ag_{1-x}SnSb_{1+x}Te_3$ system. Since a nano-phase separation is observed in the HRTEM image for $Ag_{0.85}SnSb_{1.15}Te_3$ sample (Figure 4.1), we want to see which compound in the phase diagram of this system might be the possible nano-phase observed. Accordingly we considered a number of compositions across the phase diagram: with $x = 0$ ($AgSbTe_2$), 0.2 ($Ag_2SnSb_2Te_5$), 0.25 ($Ag_3Sn_2Sb_3Te_8$), 0.333 ($AgSnSbTe_3$), 0.5 ($AgSn_2SbTe_4$) and 1.0 (Sn_4Te_4).

The $Ag_{1-x}SnSb_{1+x}Te_3$ samples were produced by John Androulakis in the group of Prof. M. G. Kanatzidis by mixing appropriate stoichiometric ratios of high purity Ag, Sn, Sb and Te. The initial charge was sealed in evacuated fused silica tubes, heated at 1000°C, held there for 4 days and then slowly cooled to room temperature. Data from the same crystal batch were used.

High energy x-ray diffraction experiments

X-ray diffraction measurements were made on the $Ag_{1-x}SnSb_{1+x}Te_3$ series of materials (Sn_4Te_4, $Ag_{0.85}SnSb_{1.15}Te_3$, $AgSbTe_2$, $AgSnSbTe_3$, $AgSn_2SbTe_4$, $Ag_3SnSb_3Te_7$, $Ag_2SnSb_2Te_5$, $Ag_3Sn_2Sb_3Te_8$, $Ag_4Sn_3Sb_4Te_{11}$) at room temperature using the RA-PDF approach described in Chapter 2 at the MU-CAT 6-ID-D beam-line at the Advanced Photon Source (APS) at Argonne National Laboratory.

X-ray powder diffraction samples were made by carefully grinding the compounds in a mortar and pestle and sieving through a 400-mesh sieve. The powders were packed into hollow flat aluminum plate sample containers with a radius of 0.25 cm and thickness of 1.0 mm, sealed between thin Kapton films.

The x-ray energy used was 87.005 keV ($\lambda = 0.14248$ Å). The data were collected using a circular image plate (IP) camera Mar345, 345 mm in diameter. The camera was mounted orthogonally to the beam path with a sample-to-detector distance of

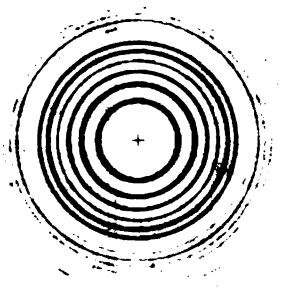

Figure 4.2: Raw diffraction data on the 2D image plate from $AgSn_2SbTe_4$. Note the excellent powder statistics.

208.86 mm which was determined by calibrating with a silicon standard sample [67].

In order to avoid saturation of the detector, each measurement was carried out by multiple exposure to the x-rays. Each exposure lasted 10 seconds, and each sample was exposed five times to improve the counting statistics. An example of the raw data on the image plate is shown in Figure 4.2. As described in Chapter 3, Fit2D and PDFgetX2 program are used to process the data. Good statistics in the high-Q region of the data allowed a $Q_{max} = 26.0$ Å^{-1} to be used which gives high-quality PDFs with good resolution.

The $F(Q)$ and $G(r)$ for all samples are plotted in Figure 4.3(a) with the corresponding $G(r)$ functions in Figure 4.3(b). The data quality are good as evidenced by

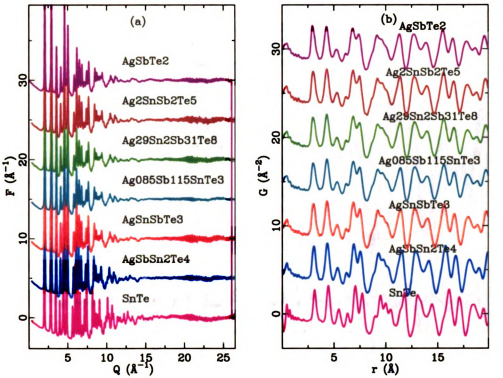

Figure 4.3: $F(Q)$ and $G(r)$ for all samples in the $Ag_{1-x}SnSb_{1+x}Te_3$ series.

the good signal-noise of the diffraction data and the low amplitude of fluctuations in the unphysical region of $G(r)$ below $r = 2$ Å in all the curves of Figure 4.3(b).

The $G(r)$ data for all the samples are plotted in Figure 4.4 on top of each other with difference curves below, where the difference curves are defined as $\Delta G(r) = G(r) - G_{SnTe}(r)$. The difference curves show fluctuations that are much larger than the estimated random errors on the data and therefore have a real origin, encoding the local structural differences between the $Ag_{1-x}SnSb_{1+x}Te_3$ and Sn_4Te_4 compounds.

Results

We would like to know whether phase separation is a bulk property for the $Ag_{1-x}SnSb_{1+x}Te_3$ system and the chemical composition and structure of the nanodomains. Accordingly we would like to search for Ag- and Sb-rich domains embedded in the SnTe matrix. Because the atomic numbers of the cations in the system are very close to each other (Ag 47, Sn 50, Sb 51), the x-ray PDF method we have used

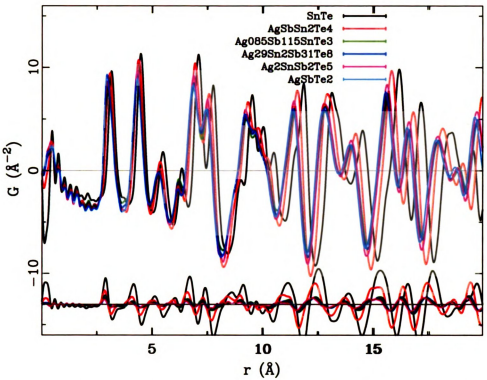

Figure 4.4: $G(r)$ and $\Delta G(r)$ (compared to Sn_4Te_4) for samples with different chemical compositions.

is not sensitive to the chemical ordering of the system. However, by simple modeling and combining the result with theory, we can still get a clue of structure, especially atomic distortions, of such a system. This was done by studying different compositions across the $Ag_{1-x}SnSb_{1+x}Te_3$ phase diagram, which might be line-compounds and participating in the nano-phase separation that is observed in $Ag_{0.85}SnSb_{1.15}Te_3$.

We fit a simple single-phase model to data from all the samples in the $Ag_{1-x}SnSb_{1+x}Te_3$ system. Fitting range is from 2.75 Å to 20 Å. Model H0 is a single phase homogeneous model of the correct average composition. In the model, the structure is NaCl like. Tellurium atoms occupy the Cl^- sites, while all the cations are distributed homogeneously on the Na^+ sites. In Table 4.1, we list the R_w and refined isotropic thermal factors on each site. The resulting lattice parameters and thermal factors for different samples are plotted as a function of x in Figures 4.5, 4.6 and 4.7.

	R_w	U_{Te} (Å^2)	$U_{Sn,Ag,Sb}$ (Å^2)
SnTe	0.097	0.0149	0.0262
$AgSn_2SbTe_4$	0.081	0.0230	0.0395
$AgSnSbTe_3$	0.088	0.0254	0.0433
$Ag_{0.85}SnSb_{1.15}Te_3$	0.114	0.0256	0.0494
$Ag_{2.9}Sn_2Sb_{3.1}Te_8$	0.097	0.0271	0.0494
$Ag_2SnSb_2Te_5$	0.090	0.0259	0.0455
$AgSbTe_2$	0.111	0.0294	0.0510

Table 4.1: Refinement result from the single-phase model to each of the samples in the $Ag_{1-x}SnSb_{1+x}Te_3$ system.

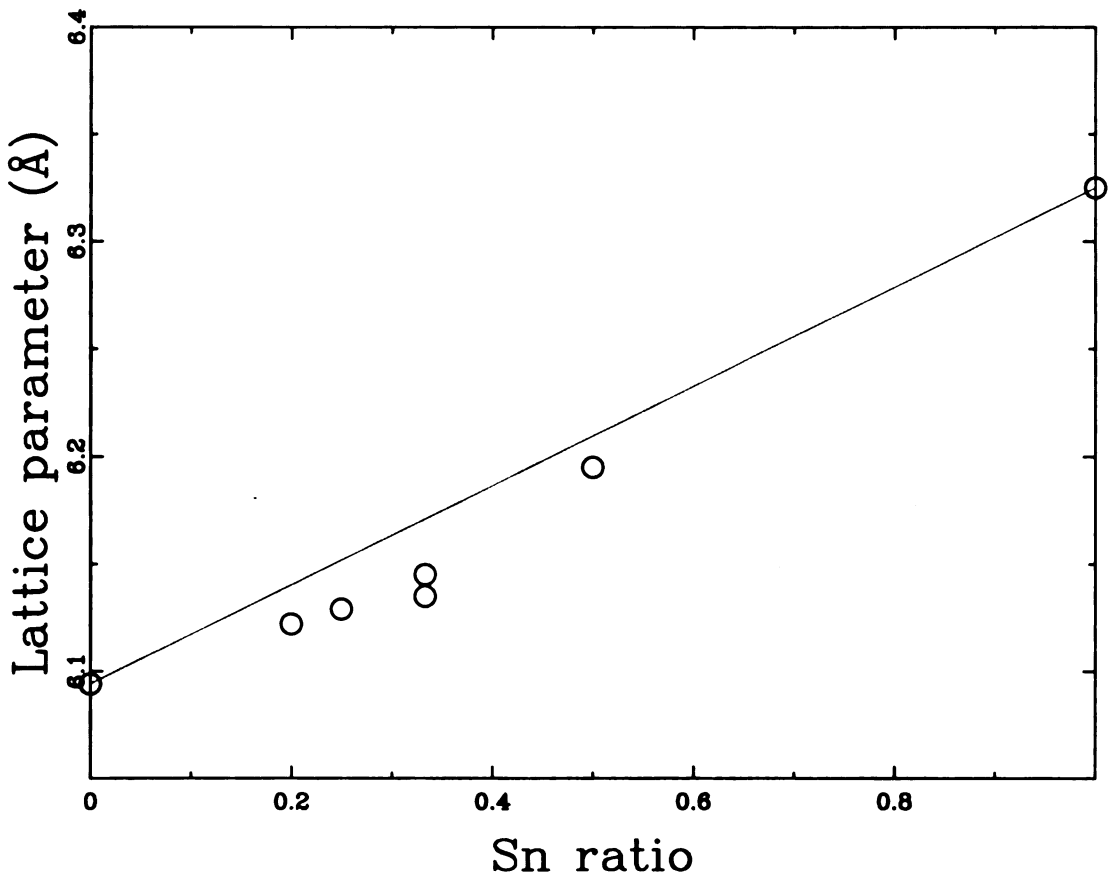

Figure 4.5: Lattice parameters from the single-phase refinements for samples with different chemical compositions in the $Ag_{1-x}SnSb_{1+x}Te_3$ series.

In each case, the homogeneous solid-solution model does a reasonable job fitting the data with small R_ws. Reasonable, though slightly large, atomic displacement factors are obtained on the anion site, but significantly enlarged ones are seen on the cation site. Note, that we are not using an ordered model, even in $AgSbTe_2$. The

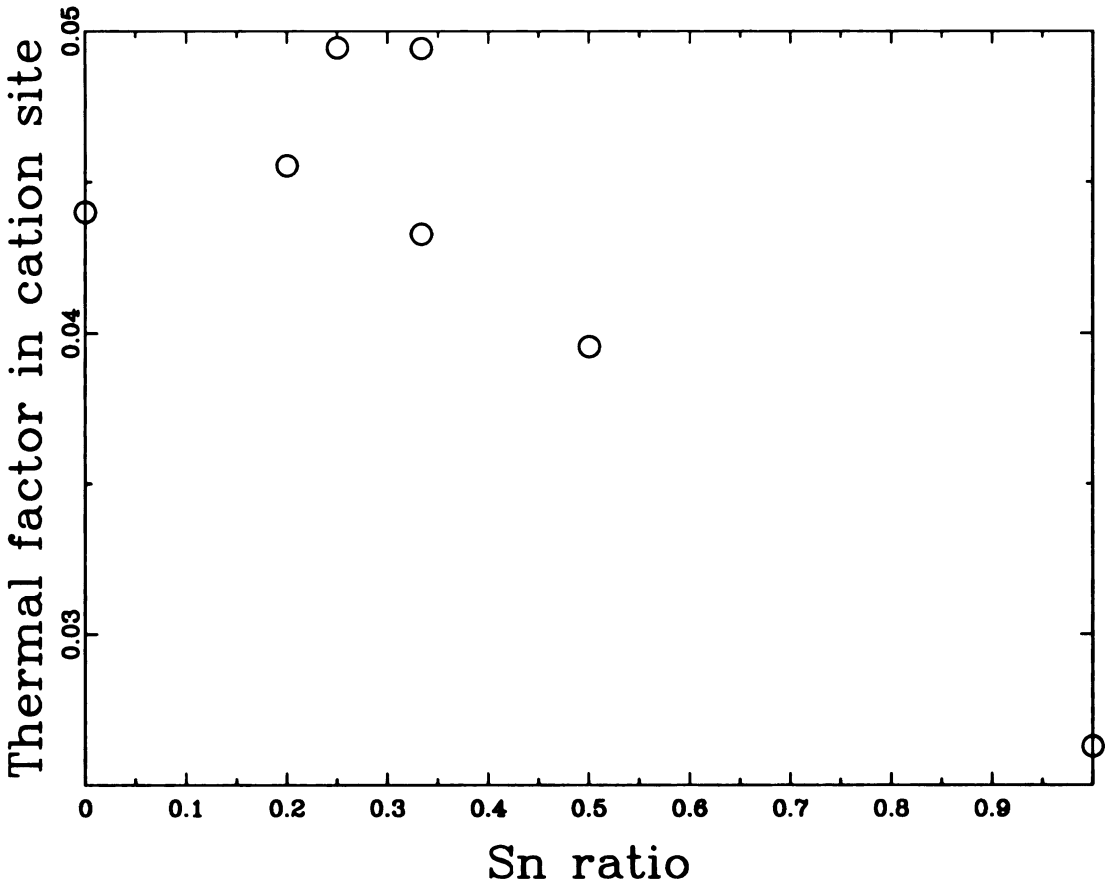

Figure 4.6: Thermal factors for the cation site from single-phase refinement for samples with different chemical composition in the $Ag_{1-x}SnSb_{1+x}Te_3$ series.

large ADPs presumably reflect the fact that the bond-lengths of Ag and Sb to Te are different but this is not allowed in the homogeneous model.

Lattice parameters obtained from one phase refinement are shown in Figure 4.5 with the Vegard's law behavior shown. The refined value has negative offset from the linear behavior of Vegard's law [90, 91]. Vegard's law is an empirical rule which says that a linear relation exists, at constant temperature, between the crystal lattice constant of an alloy and the concentrations of the constituent elements. Vegard's law applies when the solute and solvent have similar bonding properties. Deviations from Vegard's law are the norm rather than the exception and so the behavior observed here is not unusual.

In a solid solution system the thermal factors are expected to show a parabolic

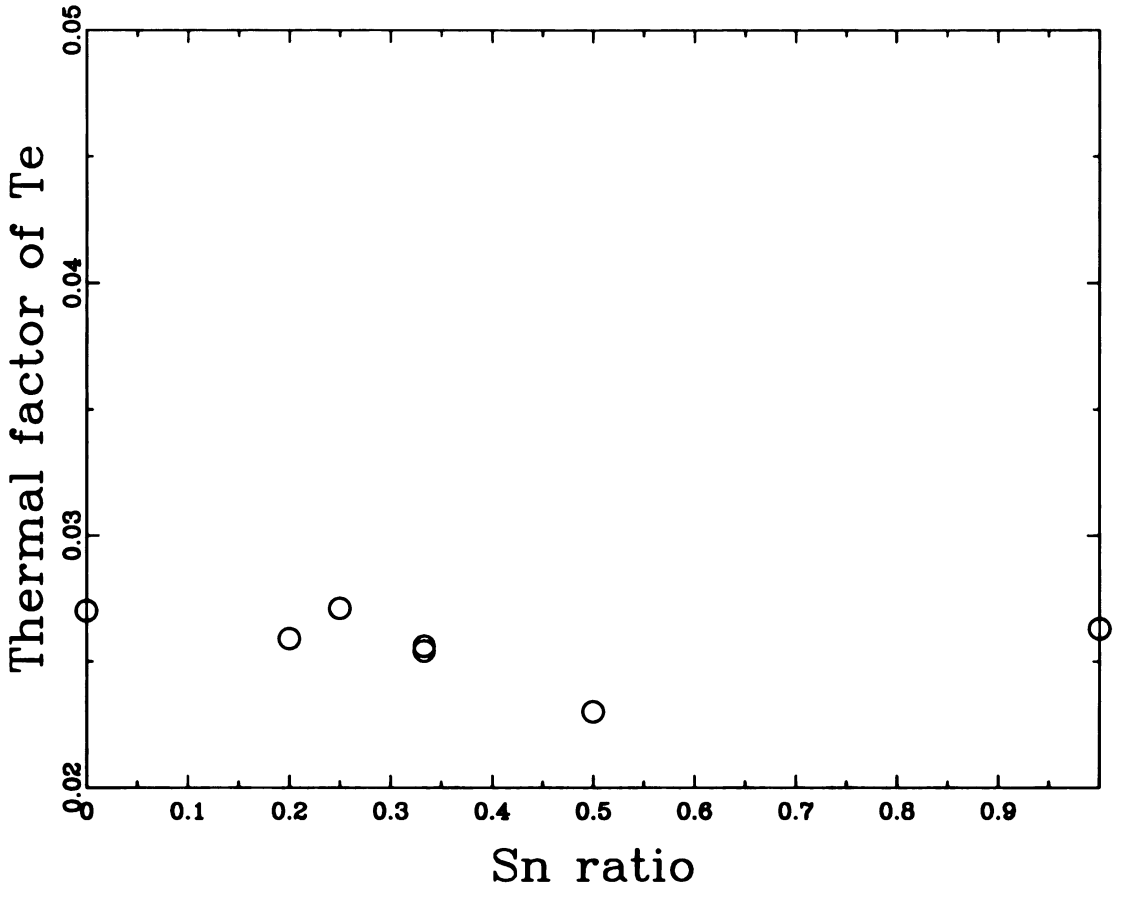

Figure 4.7: Thermal factors for the Te site from single-phase refinements for samples with different chemical composition in the $Ag_{1-x}SnSb_{1+x}Te_3$ system.

behavior with a peak at around 50%. This is qualitatively observed on the anion site (Figure 4.6, with a couple of outliers ($Ag_{0.85}SnSb_{1.15}Te_3$ and $Ag_3Sn_2Sb_3Te_8$). The anion sites have significantly smaller ADPs (Figure 4.7) and do not show parabolic behavior. These results are slightly surprising as in similar semiconductor alloy systems [92, 57] the greatest disorder is seen on the opposite sublattice to that which is being alloyed, whereas in this case the large ADPs are seen on the mixed ion sublattice with little disorder on the Te sublattice.

Thermal factors in cation sites for two samples ($Ag_{0.85}SnSb_{1.15}Te_3$ and $Ag_3Sn_2Sb_3Te_8$) appear different from others. They do not seem to follow the parabolic relation. This might mean that the structures for $Ag_{0.85}SnSb_{1.15}Te_3$ and $Ag_3Sn_2Sb_3Te_8$ samples are not solid solution. It was already found in $AgSn_2SbTe_4$ sample that phase separation

		model H_0	model $NC0_0$
R_w		0.112	0.116
Sn_4Te_4	n/n_0	-	0.02/0.333
	a (Å)	6.135	6.216
	U_{Te} (Å^2)	0.0256	0.088
	U_{Cation} (Å^2)	0.0494	0.024
$AgSbTe_2$	a (Å)	-	6.129
	U_{Te} (Å^2)	-	0.0269
	$U_{Ag,Sb}$ (Å^2)	-	0.0513

Table 4.2: Comparison of results from one-phase and two-phase refinements for $Ag_{0.85}SnSb_{1.15}Te_3$ sample.

R_w	0.114
a (Å)	6.135
U_{Te} (Å^2)	0.0258
U_{Cation} (Å^2)	0.0492

Table 4.3: Result from physically wrong model W.

does appear. So it is quite important to get HRTEM image from $Ag_3Sn_2Sb_3Te_8$ sample. It is possible that $Ag_3Sn_2Sb_3Te_8$ sample might be the line compound where chemical ordering is formed in this material. Then the nano-phase observed in $Ag_{0.85}SnSb_{1.15}Te_3$ sample might actually be $Ag_3Sn_2Sb_3Te_8$.

To explore the possibility of nano-scale phase separation we tried a number of two-phase models. Because the PDF is not sensitive to chemical ordering in this case we only tried the totally disordered case of the minor phase where $n = 0$.

Next we compare the results from single- and two-phase models to the $Ag_{0.85}SnSb_{1.15}Te_3$ sample. The results are summarized in Table 4.2. R_w from both models are reasonably good the refined values look physically reasonable.

The refined values are shown in Table. 4.2. We can see there is not much difference in the physical parameters between the two different models. The refined phase factor from the two phase model is quite unphysical. It looks like the compound is just $AgSbTe_2$but this is impossible. An explanation is that our technique is insensitive to the chemical composition. To verify this, we tried a model W with a totally incorrect

stoichiometry. We use only a single-phase model with the structure of $AgSbTe_2$. We still get a reasonable refinement result as shown in Table 4.3. This proves that our x-ray PDFs are very insensitive to chemical composition. This presents a difficulty when fitting two-phase models and so we did not pursue this further.

The amount of additional information furnished by PDF in the case of the $Ag_{1-x}SnSb_{1+x}Te_3$ was rather limited due to the similarity in x-ray scattering length of the elements involved in the alloy. This work could be pursued further in the future by combining x-ray data with neutron diffraction and PDF data, and with complementary techniques such as EXAFS.

Chapter 5

Thermoelectric PbTe/PbS system

5.1 Physics of the $(PbTe)_{1-x}(PbS)_x$ system

The thermoelectric properties of $PbTe_{0.84}S_{0.16}$ are reported to be far superior to that of PbTe [89] . The highly desirable properties of PbTe, such as its high electron mobility, are retained, but a much lower lattice thermal conductivity(0.39 W/mK, only 28% that of the PbTe at room temperature) is obtained. The system shows a $ZT \sim 1.28$ at 660 K that, it is expected, can be further enhanced by optimized doping.

A recent HRTEM study reveals spinodal decomposition happens in the PbTe composition [89]. A naturally nano-structured lattice with compositional fluctuations with a characteristic wavelength of about 2-5 nm was found. The HRTEM image is reproduced in Figure 5.1.

We can see that nano-phase separation happens on three length scales. The periodic compositional fluctuations are characteristic of spinodal decomposition [93].

The phase diagram for the $(PbTe)_{1-x}(PbS)_x$ system was obtained around 50 years ago [94, 95] and it indicates that phase separation occurs over a wide range of compositions in this system. It is reproduced in Figure 5.2. This was verified in the recent study by Androulakis *et al.* [89] and in our work, described below. For example, Fig-

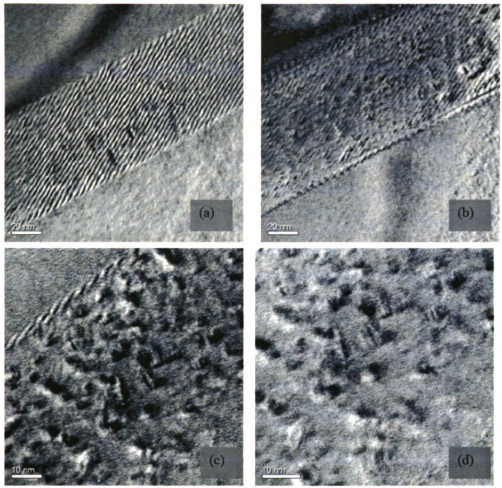

Figure 5.1: HRTEM pictures showing multi-scale phase separation happening in some part of sample. Scales are 20 nanometers in (a) and (b), and 10 nanometers in (c) and (d). [Reproduced from [89] with permission]

ure 5.3 reproduced from Reference [89] shows phase separation in a PbTe75%-PbS25% sample.

It is known that unequilibrum states of materials can be created by special heat treatment which does not allow the system to reach those equilibrium states shown in the phase diagram. In these state, the system can show interesting behavior in nano-scale. Theoretical and experimental studies suggest that materials that show nano-phase separation appear to be promising in getting a high ZT [15, 17, 96, 88]. The material with composition $PbTe_{0.84}S_{0.16}$ shows a very low room temperature

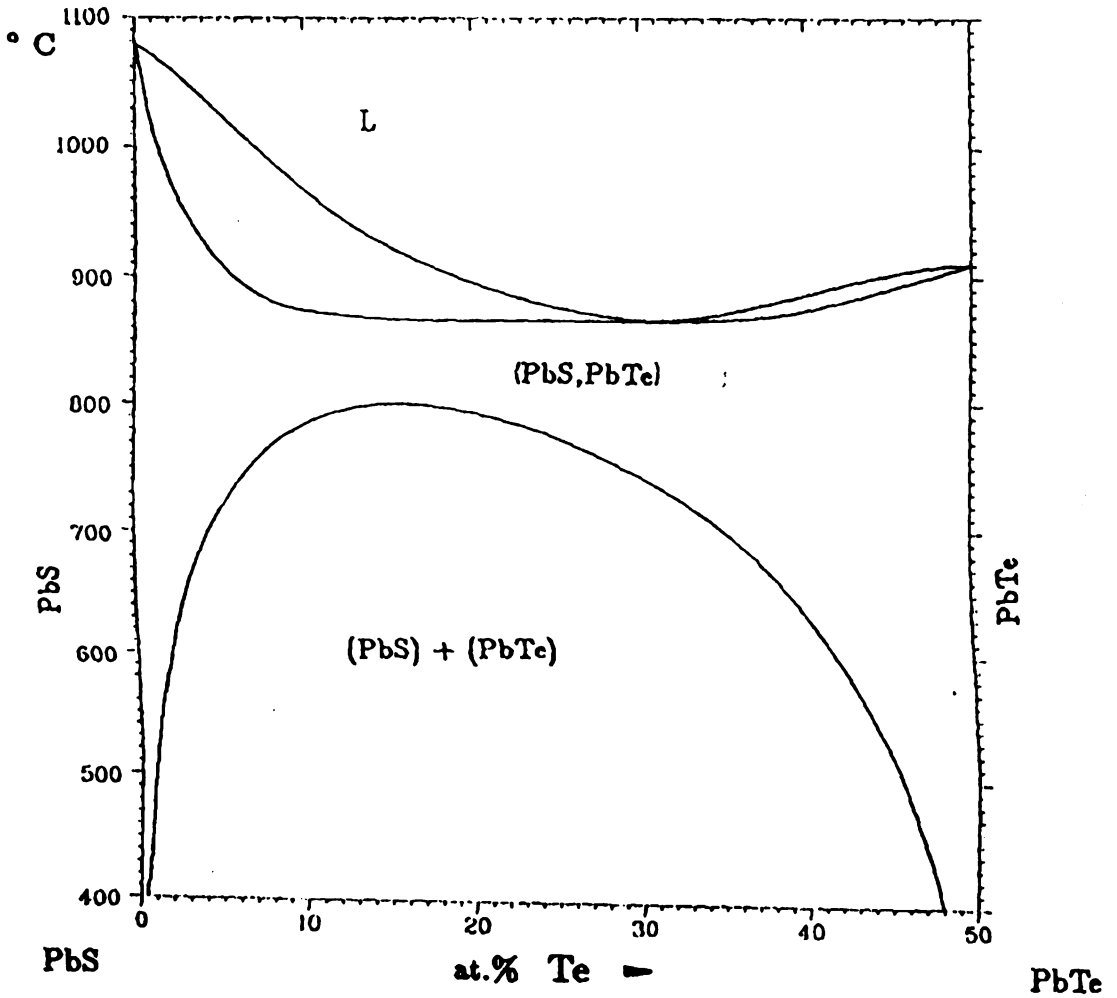

Figure 5.2: Equilibrium phase diagram for PbTe-PbS [94]

lattice thermal conductivity of 0.4 W/m K [89]. This value is only 28% of that observed in the PbTe system, which is remarkable given that the two are isostructural and $PbTe_{0.84}S_{0.16}$ has only 16 At. % of S substituted on the Te site. Understanding the origin of this remarkable reduction in κ for a small doping change should give important insights into the thermoelectric problem.

Early studies on the $(PbTe)_{1-x}(PbS)_x$ system showed that phase separation occurs at low temperature over almost the whole doping range [94, 95]. A miscibility gap exists over a wide range of composition and extends almost up to the melting point of the alloy. There are no known intermediate compounds and the phase separation occurs into phases which are almost pure PbTe and PbS over the whole alloy

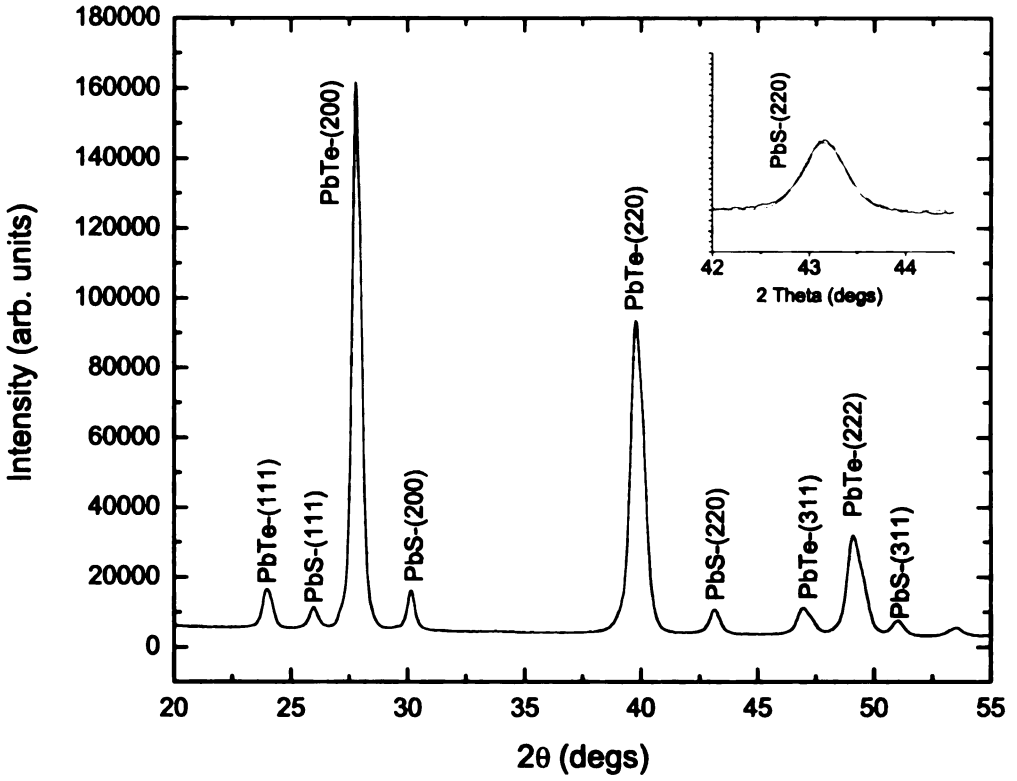

Figure 5.3: In-lab powder X-ray diffraction of PbTe75%-PbS25% sample with indices showing two phases are present of roughly PbTe and PbS composition. Reproduced from [89] with permission

range. Theoretical work [95] supports such a picture and the calculated phase diagram using a thermodynamic model agreed with the previous experimental data. Earlier work [97, 98, 99] suggested a smaller range for the miscibility gap in the phase diagram and this discrepancy was attributed to the subtle difference in chemical processing [94] and quenching rate. A high resolution transmission electron microscopy (HRTEM) study of the interesting $PbTe_{0.84}S_{0.16}$ composition revealed that spinodal decomposition happens in this system [89]. What is apparent from the TEM images is, first, that phase separation appears to be happening on different length-scales in $PbTe_{0.84}S_{0.16}$ and, second, that naturally forming striped nanostructures due to

spinodal decomposition are evident in portions of the sample. Here we investigate this question further using bulk diffraction probes of the average and local atomic structure. We address two questions. First, can we confirm that the nano-scale phase separation is a bulk property and can we characterize the average chemical composition and structure of the spinodal domain? We have also extended the study to other compositions in the phase diagram to see how these effects evolve with changing composition.

The atomic pair distribution function analysis of x-ray diffraction data is a useful method for studying nano-phase separated samples [36, 35]. In the PDF approach both Bragg and diffuse scattering are analyzed and it yields the bulk average local atomic structure. Recently it was successfully used to study the thermoelectric material, $Ag_xSbPb_mTe_{m+2}$, where silver and antimony rich nano-scale clusters were found to be coherently embedded in the PbTe matrix as a bulk property [1].

We have used both PDF and Rietveld methods to study the $(PbTe)_{1-x}(PbS)_x$ system. We find phase separation occurring over the whole composition range. Refinements from both Rietveld and PDF methods show that the $x = 0.25$, 0.5, and 0.75 samples are macroscopically phase separated into phases that are almost pure PbS and PbTe. This does not happen in the important 16% PbS doped sample. However, taking all the evidence together we suggest that the 16% sample is a nanoscale mixture of a PbTe rich phase with a partially spinodally decomposed phase of nominally 50% composition. Such a phase was stabilized and observed in a quenched $x = 0.5$ sample in this study. This offers the opportunity in the future for engineering nano- and micro-structures with favorable thermoelectric properties by controlling the thermal history in these materials.

5.2 Experimental methods

The materials were made by John Androulakis in the laboratory of professor M. G. Kanatzidis. Powder samples in the $(PbTe)_{1-x}(PbS)_x$ series were made with different compositions: $x = 0$, 0.16, 0.25, 0.50, 0.75 and 1. The samples were produced by mixing appropriate ratios of high purity elemental starting materials with a small molar percentage of PbI_2, an n-type dopant. The initial loads were sealed in fused silica tubes under vacuum and fired at 1273 K for 6 h, followed by rapid cooling to 773 K and held there over a period of 72 h. One $x = 0.5$ sample was also quenched rapidly to room-temperature. More details of sample synthesis can be found elsewhere [89].

Finely powdered samples were packed in flat plates with a thickness of 1.0 mm sealed between kapton tape windows. X-ray powder diffraction data were collected using the rapid acquisition PDF (RA-PDF) method [67], which benefits from very high energy x-rays and a two-dimensional detector. The experiments were conducted using synchrotron x-rays with an energy of 86.727 keV ($\lambda = 0.14296$ Å) at the 6-ID-D beam line at the Advanced Photon Source (APS) at Argonne National Laboratory. The data were collected using a circular image plate camera (Mar345) 345 mm in diameter. The camera was mounted orthogonally to the beam path with a sample-to-detector distance of 210.41 mm.

In order to avoid saturation of the detector, each room temperature measurement was carried out in multiple exposures. Each exposure lasted 5 seconds, and each sample was exposed five times to improve the counting statistics. Two representative 2D diffraction images for unquenched and quenched $PbTe_{0.5}S_{0.5}$ samples are shown in Figure 5.4(a) and (b), respectively. The excellent powder statistics, giving uniform rings, are evident. All the samples yielded similar quality images. The 2D Data sets from each sample were combined and integrated using the program FIT2D [77] before further processing.

Data from an empty container were also collected to subtract the container scat-

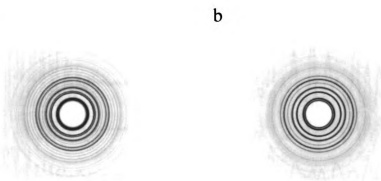

Figure 5.4: Raw x-ray powder diffraction data from the 2D detector for the $x = 0.50$ $(PbTe)_{1-x}(PbS)_x$ sample. Data from the (a) unquenched and (b) quenched samples are shown for comparison. The 1-D integrated powder diffraction patterns obtained from these data are shown in Figure 5.5(a) and on an expanded scale in Figure 5.7. The white circle in the center of each 2D difractogram represents a shadow from the beam-stop.

tering. The corrected total scattering structure function, $S(Q)$, was obtained using standard corrections [35, 67] with the program PDFgetX2 [68]. Finally, the PDF was obtained by Fourier transformation of $S(Q)$ according to $G(r) = \frac{2}{\pi}\int_0^{Q_{max}} Q[S(Q) - 1]\sin(Qr)\,dQ$, where Q is the magnitude of the scattering vector. A $Q_{max} = 26.0$ Å^{-1} was used. Setting Q_{max} to a lower value results in lower real-space resolution and higher-amplitude termination ripples and a higher Q_{max} introduces excessive statistical errors in the data since at higher values of Q the signal to noise ratio becomes unfavorable, as apparent in Figure 5.5(a). Figure 5.5, shows $F(Q) = Q(S(Q) - 1)$ and $G(r)$ for all the samples. The good statistics and overall quality of the data are apparent in Figure 5.5(a). The low spurious ripples at low-r in the $G(r)$ functions are also testament to the quality of the data [100]. Note that $G(r)$ has been plotted all the way to $r = 0$ in these plots, which is a stringent test of this.

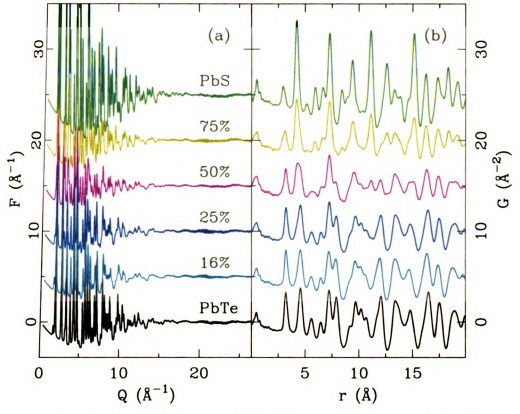

Figure 5.5: Experimental (a) $F(Q)$ and (b) $G(r)$ for all unquenched samples. In the Fourier transform, Q_{max} was set to 26.0 Å^{-1}. The data are offset for clarity. The compositions of the $(PbTe)_{1-x}(PbS)_x$ samples are indicated in panel (a). From top to bottom: $x = 1.00$ (green), $x = 0.75$ (yellow), $x = 0.50$ (magenta), $x = 0.25$ (blue), $x = 0.16$ (cyan), and $x = 0.00$ (black).

5.3 Modeling

Both PDF (using the PDFfit2 program [66, 65]) and Rietveld [32] (using the TOPAS program [101]) refinements were carried out on the system. The models used in the fits are described below.

One of the main outcomes of this study is to determine the phase composition of the phase-separated sample as a function of doping. When phase separation is long-ranged, Rietveld refinement can be used to estimate the relative abundance of the phase components [102, 103, 104, 105, 106, 107].

Phase segregation can also be determined from the PDF [1, 108]. In PDFfit2, each phase in a multi-phase fit has its own scale-factor in the refinement. The scale

factor reflects both the relative phase-fraction of the phases and the average scattering power of each phase, which depends on the chemical compositions of each phase. The conversion from scale-factor to atomic-fraction is done using the equations derived in Ref. [1].

For each sample, we tried different models. The structure is of the rock-salt type, space group Fm-3m. First we start from a homogeneous (solid solution) model where the anions are assumed to randomly distributed on the sites of the anionic sublattice. In this model, S atoms substitute the Te site randomly without breaking the symmetry. The only structural parameters refined are the lattice parameter and the thermal factors.

The next model we tried was a simple two-phase model in which a phase separation into a PbTe-rich and PbS-rich phase was assumed. The phase diagram for this system shows a miscibility gap at low temperature over a wide composition range [94, 95]. The two phases that coexist have compositions rather close to the pure end-members and there is very limited solid solubility. Based on this, and in an effort to keep the modeling as simple as possible, we modeled the phase separation as a mixture of pure PbTe and PbS; however, allowing the lattice parameters to vary as would be expected if the phases were not the pure end-members. The parameters that were allowed to vary in these fits were lattice parameters, thermal factors and phase specific scale factors which reflect the relative abundance of each phase. More complicated phase separated models were also tried where the composition of the phases was varied as described below.

5.4 Results

First we carried out PDF and Rietveld refinements on the undoped end-members of the series, PbS and PbTe. The level of agreement of Rietveld and PDFfit refinements can be seen in Figure 5.6 and Table 5.1. These fits give a baseline for the quality

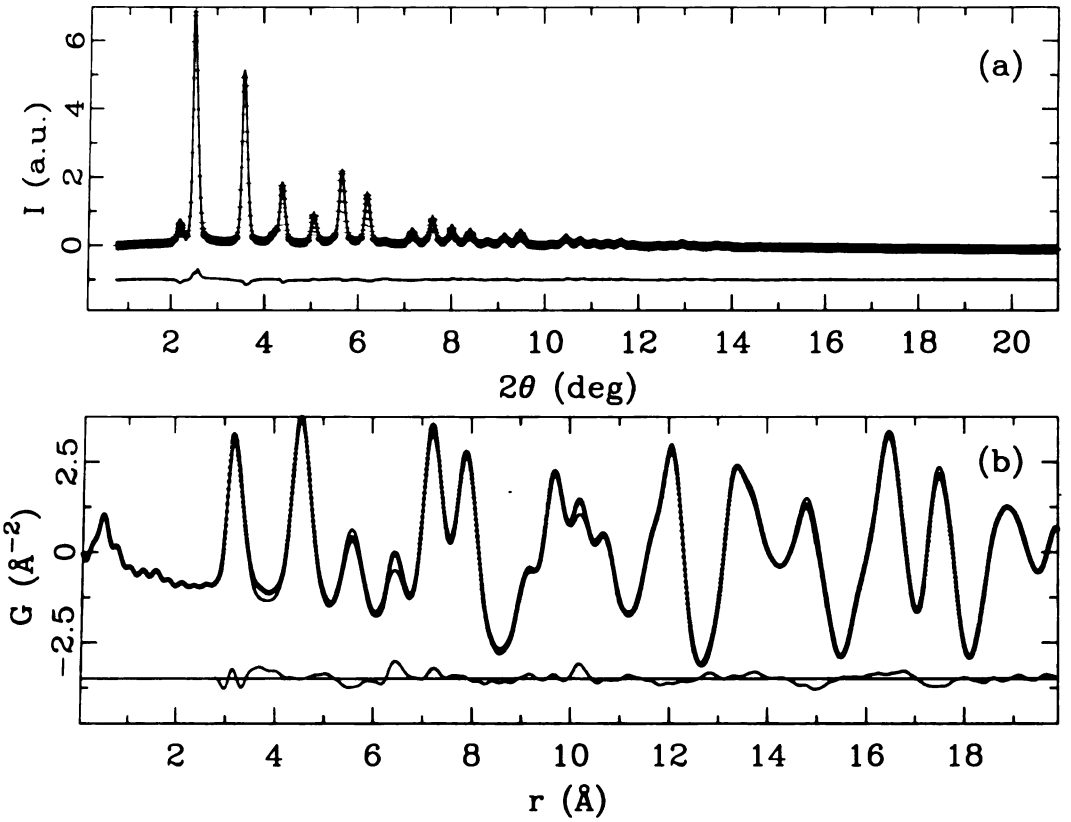

Figure 5.6: Representative refinements of the PbTe data using (a) Rietveld and (b) PDF approaches. Symbols represent data, and solid lines are the model fits. The difference curves are offset for clarity.

Table 5.1: Refinement results from PbS and PbTe compared with literature values.

	Literature[Ref. [109]]	Rietveld	PDF
R_w	-	0.03994	0.0852
a_{PbTe} (Å)	6.4541(9)	6.4776(3)	6.465(3)
U_{Pb} (Å^2)	0.0204(3)	0.033(5)	0.032(4)
U_{Te} (Å^2)	0.0141(2)	0.009(9)	0.014(4)
R_w	-	0.04377	0.0820
a_{PbS} (Å)	5.9315(7)	5.9460(3)	5.940(3)
U_{Pb} (Å^2)	0.0163(3)	0.023(3)	0.0185(5)
U_S (Å^2)	0.0156(5)	0.018(4)	0.030(5)

of the fits for materials without disorder. The fits are acceptable and the refined parameters are in reasonable agreement with literature values for PbTe, though outside the estimated errors. This reflects in part that the samples were different, and also the fact that systematic errors are not accounted for in the error estimates. The PDF and Rietveld refinements are also only in semi-quantitative agreement. The pa-

rameter estimates were made on the same data-sets but using different methods and, again, systematic errors are not accounted for in the error estimates. Even in these nominally pure materials the refined thermal factors are rather large [110], which is in agreement with previous work [109].

Now we consider the chemically mixed systems. The existence of phase separation can be *qualitatively* verified in our samples by looking at the diffraction patterns in Figure 5.7. The top curve is PbS and the bottom curve is PbTe and the vertical dashed lines are at the positions of the main Bragg-peaks of these phases. Despite the low-resolution of the data, a characteristic of the RAPDF measurement [67], for compositions $x = 0.25$, 0.50 and 0.75 a coexistence of PbS and PbTe diffraction patterns is clearly evident as the diffraction patterns are qualitatively recognizable as a linear superposition of the end-member patterns. Diffraction peaks appear at precisely the positions of the end-member Bragg-peaks. The same is true for the annealed $x = 0.5$ sample (dark magenta). On the other hand, the *quenched* $x = 0.5$ sample has a diffraction pattern that resembles the PbTe pattern but shifted significantly to the right. This is what would be expected for a solid-solution, rather than phase separated, sample suggesting that quenching the sample suppresses phase separation.

The situation is slightly less clear for the $x = 0.16$ sample which resembles closely the pure PbTe diffraction pattern. The effects of phase separation would be difficult to see in this case because of the small PbS component. However, careful inspection of the curve indicates that the main peaks are shifted to the right, in analogy with the quenched $x = 0.5$ sample. We thus conclude that this sample is a solid-solution on the macro-scale probed in a diffraction pattern.

We would like to consider evidence in the *local* structure for phase separation. The PDFs of the data in Figure 5.7 are shown in Figure 5.8 arranged in the same way and with the same colors as they are in Figure 5.7. The samples that are macroscopi-

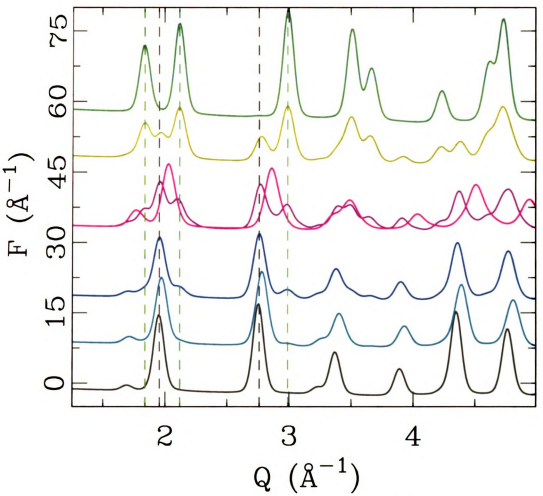

Figure 5.7: The low-Q diffraction patterns of all the $(PbTe)_{1-x}(PbS)_x$ samples studied, where $F(Q) = Q(S(Q)-1)$. From top to bottom: $x = 1.00$ (green), $x = 0.75$ (yellow), $x = 0.50$ (light and dark magenta), $x = 0.25$ (blue), $x = 0.16$ (cyan), and $x = 0.00$ (black). The data corresponding to the quenched $x = 0.50$ sample (light magenta) is superimposed on top of that of the unquenched sample (dark magenta) without being offset. The other data are offset for clarity. Vertical dashed lines indicate positions of several characteristic Bragg peaks in the endmember data to allow for easier comparison.

cally phase separated ($x = 0.25$, 0.5 (annealed) and 0.75) also show phase separation tendencies in the local structure as expected, the curves having the qualitative appearance of a mixture of the end-member PDFs.

The behavior of peaks in the PDF in solid-solutions has been discussed previously [92, 57]. The nearest neighbor peaks retain the character of the end-members, albeit with a small strain relaxation. However, peaks at higher-r, from the second-

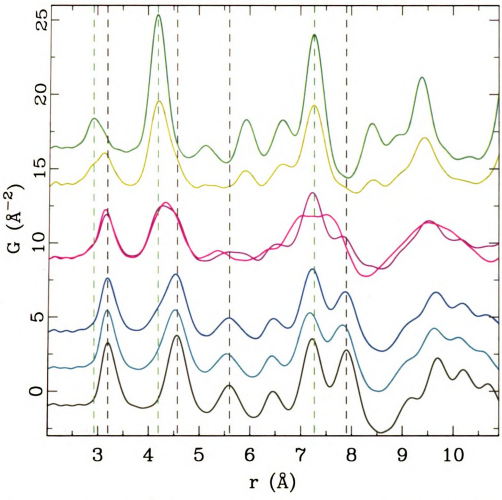

Figure 5.8: Experimental PDFs for various $(PbTe)_{1-x}(PbS)_x$ samples on expanded scale. The PDFs, from top to bottom correspond to $x = 1.00$ (green), $x = 0.75$ (yellow), $x = 0.50$ (magenta), quenched $x = 0.50$ (bright magenta), $x = 0.25$ (blue), $x = 0.16$ (cyan), and $x = 0.00$ (black). The data corresponding to the quenched $x = 0.50$ sample (light magenta) is superimposed on top of that of the unquenched sample (dark magenta) without being offset. The other data are offset for clarity. Vertical dashed lines indicate positions of a few selected characteristic PDF features of the endmembers for easier comparison.

neighbor onwards, appear broadened because of inhomogeneous strain in the sample but are peaked at the average position expected for the virtual crystal model. The $x = 0.5$ (quenched) and $x = 0.16$ samples follow this behavior even on the 1 nm length-scale suggesting that they are solid-solutions even on the local scale.

To investigate the phase separation phenomenon more quantitatively, we carried out two-phase refinements for the macroscopically phase separated samples on both

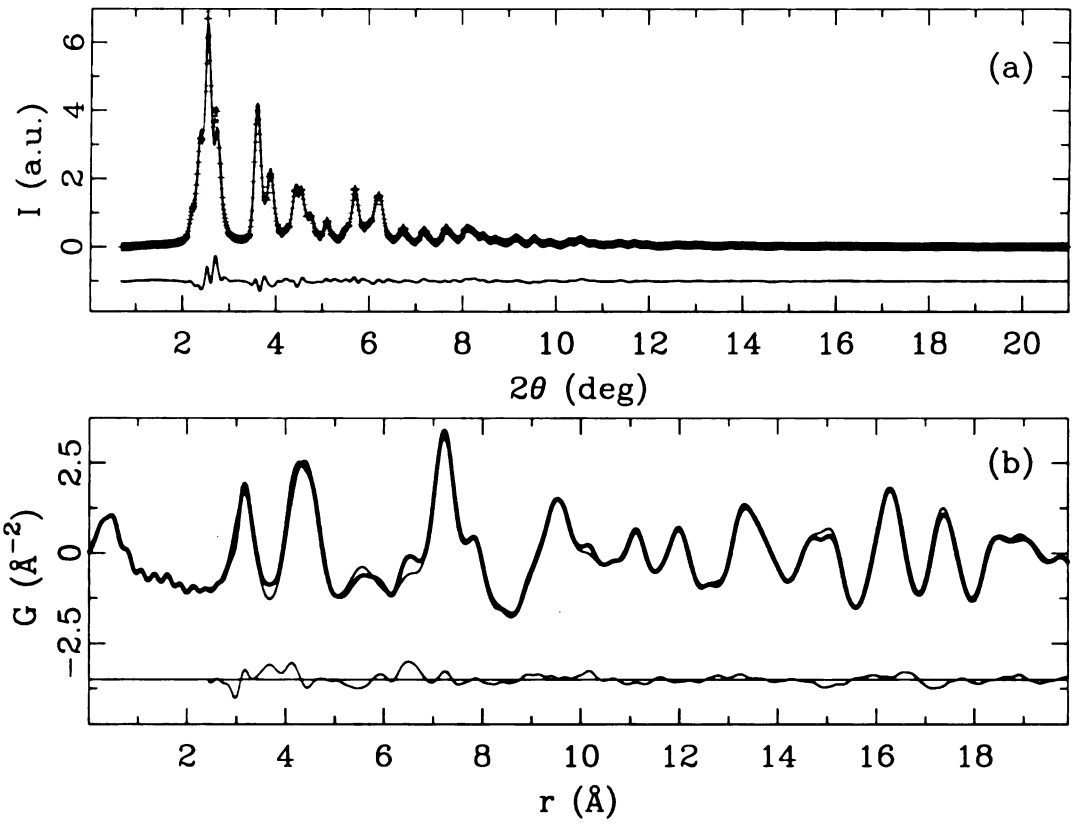

Figure 5.9: Representative refinements of the $x = 0.50$ sample data using (a) Rietveld and (b) PDF approach. Symbols represent data, and solid lines are the model fits. The difference curves are offset for clarity.

the diffraction data and the PDF. Figure 5.9 shows representative fits from the $x = 0.50$ sample. The refined parameters are reproduced in Table 5.2. In the table the n and n_0 refer to the refined fraction of the sample in the PbTe phase and the expected fraction based on the stoichiometry and assuming phase separation into pure PbTe and PbS, respectively. The two-phase fits using pure PbS and PbTe as the two phases are good ("Rietveld" and "PDF" columns in the table), as indicated by the low residuals that are comparable to the end-member fits. The refined atomic displacement parameters (ADPs) are also in good agreement with the end-member refinements, though the refinements of this parameter are somewhat unstable on the PbS phase when it is the minority phase as it does not contribute strongly to the scattering in that case. The result that relatively large ADPs are needed on the Pb site in PbTe and on the S site in PbS are reproduced in the two-phase fits of the

Table 5.2: Refinement results for two-phase fitting. "Rietveld" and "PDF" refer to Rietveld and PDF fits, respectively, where the composition of the two phases was fixed to PbTe and PbS. n and n_0 refer to the refined and expected (based on stoichiometry) phase fractions for the PbS-rich phase

	25%		50%		75%	
	Rietveld	PDF	Rietveld	PDF	Rietveld	PDF
R_w	0.03427	0.118	0.0468	0.151418	0.03385	0.0996
n/n_0	0.19/0.25	0.20/0.25	0.50/0.50	0.49/0.50	0.71/0.75	0.80/0.75
C	6.4669(3)	6.446(3)	6.4418(3)	6.414(3)	6.4301(3)	6.415(3)
U_{Pb} (Å^2)	0.037(6)	0.040(4)	0.041(6)	0.040(5)	0.040(7)	0.040(5)
U_{Te} (Å^2)	0.015(6)	0.016(4)	0.0052(6)	0.019(4)	0.033(7)	0.02(4)
a_{PbS}(Å)	5.9768(3)	5.97(1)	5.9841(3)	5.953(4)	5.9738(3)	5.956(3)
U_{Pb} (Å^2)	0.044(8)	0.027(5)	0.034(7)	0.025(4)	0.024(6)	0.023(3)
U_S (Å^2)	0.073(8)	0.03(5)	-0.0027(7)	0.031(4)	0.0065(6)	0.029(3)

phase separated samples.

The lattice parameters of the PbTe in the phase separated samples are consistently shorter than for the pure material, and they are consistently longer for the PbS phase component. This effect is real and reflects the fact that the phases in the phase separated samples are actually solid-solutions with finite amounts of S in the PbTe and Te in the PbS phase, respectively. We can make a rough estimation of the composition of the phase separated phases by considering their refined lattice parameters and assuming that Vegard's law [90, 91] is obeyed in the vicinity of the end-member compositions. In this case, the formula for the lattice parameter in the solid solution of composition $PbTe_{(1-y)}S_y$ is $a_y = y(a_{PbTe}) + (1-y)a_{PbS}$. Thus, we can estimate the compositions of the solid-solutions in the phase separated phases from the Rietveld refined lattice parameters. We find that in the $x = 0.25$ phases, $y = 0.94$ for the PbS rich phase and $y = 0.05$ for the PbTe rich phase. This verifies that the composition of the phases in the two-phase mixture are indeed very near PbTe and PbS. The values determined from the $x = 0.5$ and 0.75 samples give the same result with the estimated composition of the PbTe-rich phase as $y = 0.895$ and that of PbS $y = 0.03$. This suggests that the solid solubility limit is in the region 3-10% at both ends of the phase diagram.

The powder diffraction data are relatively insensitive to small changes in chemical composition of the particular phases [108] which explains the good fit to the data with the endmember PbS and PbTe compositions, albeit with modified lattice parameters. However, for completeness we have carried out two-phase refinements to the phase separated data using the nominal compositions for the two phases that were determined above. The fits were comparable to those where the composition of the two phases were limited to pure PbTe and PbS but with more physical ADPs being refined on the PbS component.

The agreement of the refined with the nominal composition, n/n_0, is best in the $x = 0.50$ sample in both the PDF and Rietveld data. It is less good, though acceptable for the 0.25 and 0.75. Due to the relative insensitivity to chemical composition we expect rather large error bars on these quantities and don't ascribe significance to the differences. The agreement between the Rietveld and PDF results shows that the phase separation is macroscopic since we get the same result in both the local and average structures.

We now consider the samples that appear from the qualitative analysis of the data to be solid-solutions: $x = 0.5$ (quenched) and $x = 0.16$. In Figure 5.10 we consider the $x = 0.5$ sample. In this figure, model PDFs of the undoped endmembers are reproduced for reference and the positions of their main peaks are marked. The quenched data are shown as grey symbols in the cuves (c) and the annealed data in the curves (d). The magenta lines are simulated PDFs. In (c) the simulated PDF is from a homogeneous solid-solution virtual-crystal model with the right nominal composition and lattice parameter. It agrees well with the data. In (d) the simulated PDF is a linear combination of the PbTe and PbS PDFs. In each case the ADPs of the simulations have been adjusted to give the best agreement with the data. The simulations fit rather well indicating that this picture of phase separation (annealed) vs solid solution (quenched) is a good explanation of the bulk behavior for the $x = 0.5$

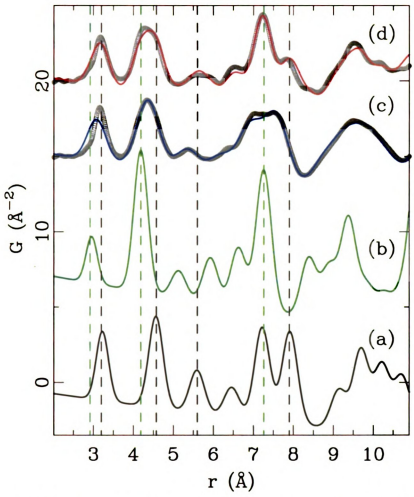

Figure 5.10: PDFs of converged models for (a) $x = 0.00$ and (b) $x = 1.00$ $(PbTe)_{1-x}(PbS)_x$ samples. Comparison of the data for (c) quenched and (d) unquenched $x = 0.50$ samples (open symbols) with the solid solution (c) and mixture (d) models (solid lines), respectively. See text for details. Vertical dashed lines indicate positions of selected PDF features characteristic for the endmember compositions, for easier comparison.

sample. Quantitative refinement results for the quenched 50% sample are reproduced in Tab. 5.3 The fits are good with low R_w's and reasonable refined parameters. The refined lattice parameter is between the end-member values as expected and the ADP on the lead-site is further enlarged from the endmember values as expected due to disorder in the alloy.

In the quenched $x = 0.5$ sample the solid-solution is not thermodynamically stable but is metastably trapped by the rapid quench. The quench is very successful

Table 5.3: Refinement results from both PDF and Rietveld for the quenched 50% sample from a homogeneous solid-solution model.

	Rietveld	PDF
R_w	0.047	0.163
a (Å)	6.2571(4)	6.217(3)
U_{Pb} (Å^2)	0.055(5)	0.062(3)
$U_{Te,S}$ (Å^2)	0.017(5)	0.054(3)

at suppressing phase separation as discussed above. However, it is not completely successful, as TEM images of the quenched $x = 0.5$ sample indicate that the sample has compositional modulations, as shown in Figure 5.11(b). The striped nature of these modulations suggests that there is an arrested spinodal decomposition taking place in the 50% doped sample, that would result in sinusoidal compositional modulations about the nominal 50% composition. The amplitude of the modulations are not known, but the good agreement of the homogeneous solid-solution model to the PDF and Rietveld data suggest that the variation in composition around the nominal 50% is not too large.

Thus we understand the quenched 50% sample to be close to an ideal metastable solid solution, but with an arrested spinodal decomposition that gives rise to nanoscale compositional modulations.

Of greater interest from both a technological and scientific viewpoint is the behavior of the $x = 0.16$ sample that shows especially good thermoelectricity. As discussed above, the diffraction data in Fig 5.7 suggests that the sample is macroscopically a solid solution even though it lies outside the range of solid solubility suggested by the phase diagrams [94, 95] and inferred from the composition of the PbTe-rich phase of the phase-separated compositions in our own refinements (25%, 50%, 75% sample).

We tried fitting two-phase and homogeneous models to both the diffraction and PDF data. The results are shown in Table 5.4 and Table 5.5 with representative fits shown in Figure 5.12. As expected from the qualitative analysis of the data discussed above, the single-phase solid-solution model (model A) provides acceptable fits to the

		model A		model B	
		Rietveld	PDF	Rietveld	PDF
	R_w	0.04647	0.1209	0.05186	0.121
	n/n_0	-	-	0.14/0.16	0.037/0.16
PbTe	a (Å)	6.4264(5)	6.403(3)	6.4233(4)	6.403(24)
	U_{Pb} (Å^2)	0.047(5)	0.047(3)	0.035(6)	0.035(3)
	U_{Te} (Å^2)	0.0061(6)	0.019(3)	0.023(6)	0.029(4)
second phase	a (Å)	-	-	5.900(1)	5.942(4)
	U_{Pb} (Å^2)	-	-	0.018(8)	0.021(6)
	$U_{S,Te}$ (Å^2)	-	-	0.013(8)	-0.0024(6)

Table 5.4: Rietveld and PDF refinement results from three different models for the $PbTe_{0.84}S_{0.16}$ sample: model A is solid solution model, model B is a simple two-phase mixture of PbTe and PbS. n and n_0 refer to the refined and expected (based on stoichiometry) phase fractions for the PbS-rich phase.

		model C	
		Rietveld	PDF
	R_w	0.03068	0.114
	n/n_0 0.31/0.32	0.24/0.32	
PbTe	a (Å)	6.4203(4)	6.416(3)
	U_{Pb} (Å^2)	0.028(6)	0.036(4)
	U_{Te} (Å^2)	0.016(6)	0.025(5)
second phase	a (Å)	6.1673(3)	6.255(3)
	U_{Pb} (Å^2)	0.253(8)	0.064(6)
	$U_{S,Te}$ (Å^2)	0.253(8)	0.070(6)

Table 5.5: Model C is a mixture of pure PbTe phase plus a solid solution of composition $PbTe_{0.5}$-$PbS_{0.5}$.

data. The refined lattice parameters are shorter than pure PbTe. According to the Vegard's law analysis, the refined lattice parameter gives a nominal composition for this sample of 0.14 (Rietveld)/0.12 (PDF), in reasonable agreement with the actual composition. Enlarged ADPs are found on the Pb sublattice with smaller ADPs on the Te lattice, as was the case for the PbTe end-member. As expected for a solid-solution, the ADPs are enlarged with respect to PbTe.

For completeness, we also tried the simple model of phase separation into pure PbTe and PbS end-members. The results appear in Table 5.4 as model B. The Rietveld fit is significantly worse as measured by R_w. In the case of the PDF fit the

R_w is comparable but the refinement reduced the phase fraction of the second phase and adjusted the lattice parameter of the majority phase, moving the refinement back towards the solid-solution result. This refinement also returned unphysical negative atomic displacement factors on the minority phase. The solid-solution model is clearly preferred over full phase separation from the bulk diffraction measurements.

The TEM images from the 16% sample (Ref. [89] and Fig. 5.11(a)) suggest that it is two-phased, with one phase being homogeneous and the other resembling the quenched $x = 0.5$ sample with arrested spinodal decomposition. A model that simulated this situation was successful compared to the PDF data, as shown from model C in Table 5.5. This model assumed that the nominally 16% sample is phase separated into regions that are pure PbTe and regions that resemble the quenched 50% sample, i.e., they are nominally $x = 0.5$ solid-solutions but also exhibiting spinodal decomposition as suggested by the TEM images. Thus, model C is a phase separation into pure PbTe and a solid solution of composition $PbTe_{0.5}S_{0.5}$. This model gives the lowest R_w's for fits to the 16% compound in both the Rietveld and PDF refinements. The phase fractions were free to vary but refined to values that are close to those expected. The lattice constants refined to reasonable values. The majority phase lattice constant was close to that of the PbTe rich phase in the two-phase refinements in Table 5.2. In the case of the minority phase, the lattice constant lay between pure PbTe and PbS consistent with a nominal 50% composition. The ADPs are slightly large in the PbTe-rich phase but physically reasonable. In the minority phase the ADPs are unphysical in the Rietveld refinement suggesting that this parameter is not well determined in the refinement. However, in the PDF refinement they are more reasonable, but very large. This is perfectly consistent with the fact that this minority phase itself actually has a compositional variation due to the spinodal effects.

5.5 Summary

This work confirmed the phase separation tendency of the PbTe/PbS system. It also showed that phase separation can be effectively, but not completely, suppressed by quenching at 50% composition, where a partial spinodal decomposition appears to be taking place, at least in a portion of the sample.

However, the main result is an improvement in our understanding of the state of the technologically promising 16% sample. Measurements of the bulk average structure, and the bulk local structure, indicate that it is not phase separated into PbTe-rich and PbS-poor endmembers like the other similarly processed samples in the series. The best explanation of all the data at hand is that this sample prefers a phase separation into a PbTe-rich phase and a phase that is nominally 50% doped, but which has a partial spinodal decomposition reminiscent of the quenched 50% sample. Such a nano-scale phase separation is thought to be important in producing the very low lattice thermal conductivity κ that is observed in this material [89]. Interestingly, in this case the effect appeared not after a quench, but after an anneal, suggesting that it might be the thermodynamically preferred state, though this needs to be investigated further.

The other important observation from this work is that quenching is very important in determining the phase separation and resulting nano-scale microstructure. This suggests that in this system it may be possible to engineer κ, and therefore ZT in the bulk material by appropriate heat treatments. This is a promising route for future research.

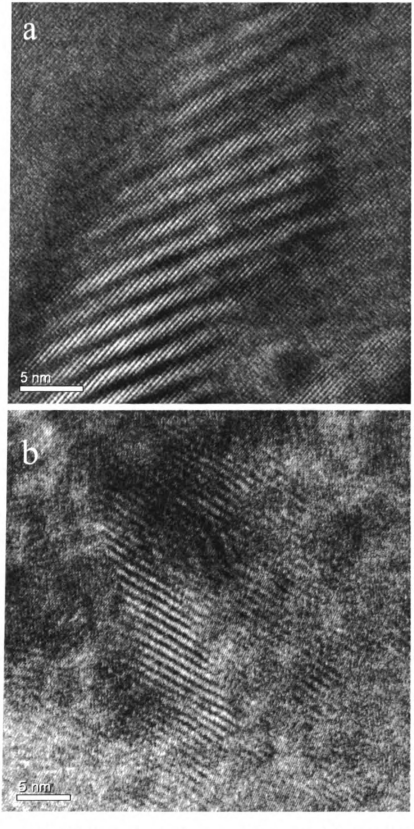

Figure 5.11: HRTEM images of (a) $x = 0.16$ and (b) quenched $x = 0.50$ $(PbTe)_{1-x}(PbS)_x$ samples.

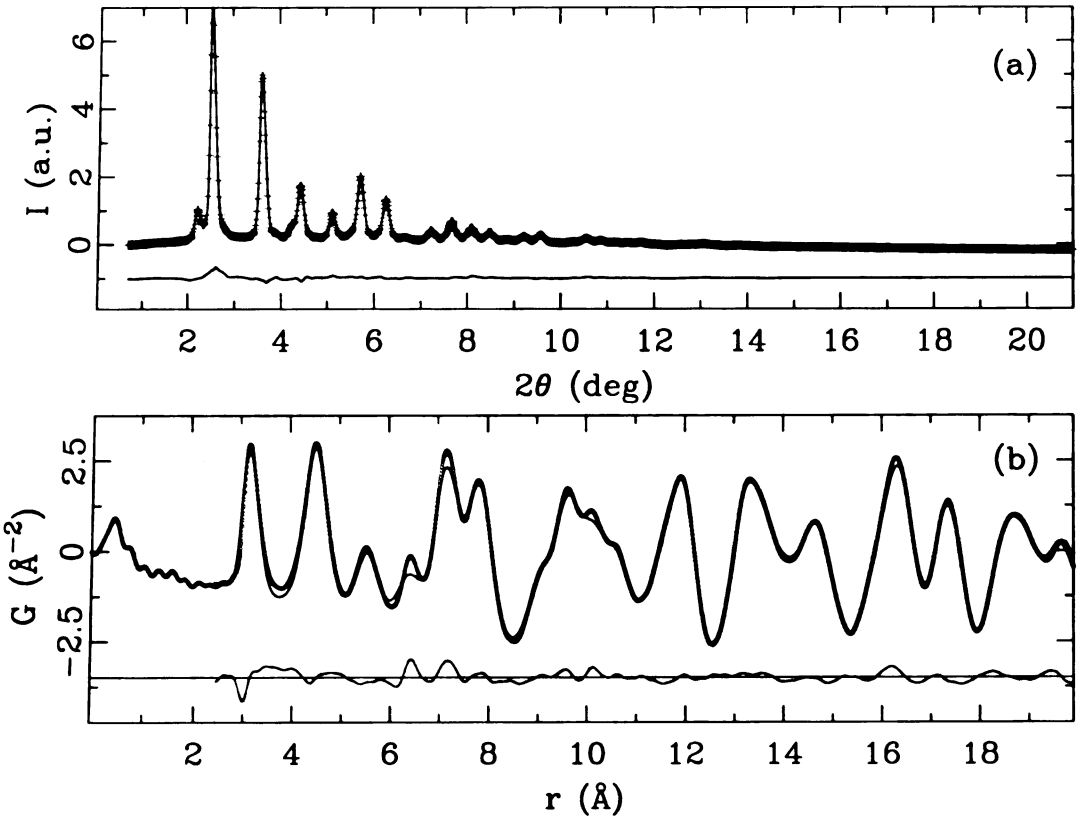

Figure 5.12: Representative refinements of the $x = 0.16$ sample data using (a) Rietveld and (b) PDF approach. Symbols represent data, and solid lines are the model fits. The difference curves are offset for clarity.

Chapter 6

Concluding Remarks

6.1 PDF analysis of new thermoelectric materials

We set out to determine the local structure of novel thermoelectric materials, using the atomic pair distribution function (PDF) method [35] and combining other experimental methods.

The goal of this study was to understand the origin of the unusual thermoelectric properties in these novel materials from the structural aspect, and to provide the feedback people in materials engineering need to synthesize new materials with ZT suitable for industrial applications.

A common feature is found in these studied materials, which is the presence of nanoclusters in bulk material. In the $AgPb_mSbTe_{m+2}$ system where high ZT was found, nanoclusters with average chemical composition $AgPb_mSbTe_{m+2}$ were found embedded in the PbTe matrix. In the $(PbTe)_{1-x}(PbS)_x$ system where the extremely low thermal conductivity was found, nanoclusters with average chemical composition of PbTe were found in the representative material PbTe75%-PbS25%. In the $Ag_{1-x}SnSb_{1+x}Te_3$ system, although the current PDF data are not sufficient in drawing a conclusive result about the chemical composition of the nanoclusters, the trace of nanoclusters is found by studying the HRTEM pictures and by the preliminary

analysis of PDF data. Although very strong arguments like 'these nanoclusters directly cause such unusual thermoelectric properties' can not be clearly made at this current moment, we do expect that there must be a close connection between these nanoclusters and these unusual thermoelectric properties.

A deep and precise understanding of how, physically, such nanostructures give rise to these unusual transport behavior, especially in a quantitative way, needs much further work. Computer simulations are needed to understand the transport phenomena and their relationship to the nanoscale structures we have studied here. With the emergence of high performance computing and daily-increasing computing power of PCs, we look forward to seeing fruitful results from theory and simulation in the future in these interesting new materials.

Experimentally, many further detailed research work needs to be done. How to control the cluster size? How cluster size affect the figure of merit ZT? Of course more systematic studies need to be carried on in these systems. There is a still very long way to go for thermoelectric material study. This thesis only shows a path or a direction to go.

PDF played a central role in our study of such nanoscale structure problem. Its power is shown in our analysis procedure. Qualitative results from PDF are easily and intuitively drawn directly from the data, with quantitative modeling providing valuable additional information. We expect to see more applications of the PDF method in the study of such nanoscale structure problems.

6.2 Alternative approaches and future work

6.2.1 Alternative approaches

In this subsection, other experimental methods helpful in solving the structure of these materials are listed. These are complementary experimental methods and are

supposed to provide complementary information on material structures that PDF is not sensitive to. These methods are either already tried or could be tried later.

EXAFS

Extended X-ray Absorption Fine Structure (EXAFS) method was tried on $Ag_{0.86}Pb_{18}SbTe_{20}$ sample. EXAFS is the oscillating part of the X-ray Absorption Spectrum (XAS) that extends to about 1000 eV above an absorption edge of a particular element of a sample. It gives us the nature of the neighboring atoms surrounding the selected central atom (their approximate atomic number). EXAFS is a complementary method for PDF, since PDF is not very sensitive to the chemical ordering especially when the atomic numbers of the compositional elements are close to each other. It is difficult to distinguish different models using the PDF method in which the only difference between models comes from the substitution of atoms with near atomic numbers . As described in Ref. [1], we give an estimation of the average chemical composition for the second phase, but we cannot totally decide the chemical ordering in the second phase. We tried EXAFS to solve this problem. Although theoretical calculations are very complicated for EXAFS, the computer software for approximate calculation is already available. Data for $Ag_{0.86}Pb_{18}SbTe_{20}$ sample was collected. K edges for Ag and Sb element were tried. Detailed analysis can be found in the report [111]. The result from EXAFS is not conclusive for this specific material. One reason is that Sb, Ag have very close atomic numbers (less than 5). The other is that theoretical calculations involving more shells are needed to distinguish the different models. However, experimental EXAFS signal can only go as far as 5 Å, thus the signal from experiment is not enough to distinguish the different chemical ordering models we tried.

Anomalous X-ray scattering

Another promising method to study the chemical ordering is the anomalous X-ray scattering method. The experiment uses an x-ray energy near the resonant edge of the selected element in the sample. The scattering factor of an atom is nearly independent of the energy of x-rays except in the vicinity of the absorption edge of the atom where it depends rather strongly on the X-ray energy E. By carrying out the measurement at two or more energies in the vicinity of the edge of the element α, the scattering power $f_\alpha(Q)$ of the α atoms change but those of the other constituent ions don't. The idea is to measure two energies, one near the absorption edge, the other far from the edge. The difference in specific peaks of the two PDFs thus derived will show the contributions from this special element and thus provide information on the distribution of the element in the materials. This provides information on chemical ordering which is usually not very sensitive in the regular PDF method. This approach has been demonstrated [112] but difficulties in carrying out the measurements make it far from commonplace. However, it is a promising approach for the $Ag_{1-x}SnSb_{1+x}Te_3$ project. More detailed description, including math formula, can be found in the book [35]. This method is a quite promising experimental technique, and will certainly gain more and more broad application in wide field of material science if it is further developed.

6.2.2 Future Work

6.2.3 Obtaining PDFs using other source and detector

PDF data with higher Q space resolution are needed for the project $Ag_{1-x}SnSb_{1+x}Te_3$ as described before in Chapter 4. Two types of experiment can be done for such a purpose. One is to use the solid state detector in an x-ray experiment and scan to wider diffraction angles. The other is to use a neutron source. These experiments

take longer than the RAPDF measurements to collect data and we only do them now when there is sound reason to conduct such experiment, that is when they provide needed information which other experiment like RAPDF can not provide. It is not completely clear that higher resolution is warranted in this case.

The other simple way to determine whether there is two phase separation happening or nanophase exists in bulk material is to determine the size of the clusters. To determine the size of the clusters, it would be good to consider the PDF over a wider r-range. Q resolution affects the height of the PDF signal and determine how far we can go in the r range and this would require a new set of experiments with PDFs determined from higher resolution diffraction data. Using the refinement results obtained from the low r range and consecutively evolve into the high r range, we can approximately estimate in which length scale the PDF refinement give unphysical result and that length scale will be around the cluster size. This consequent refinement method is already implemented in the new PDFGUI [66] program.

Bibliography

[1] H. Lin, E. S. Božin, S. J. L. Billinge, E. Quarez, and M. G. Kanatzidis, **Nanoscale clusters in the high performance thermoelectric $AgPb_mSbTe_{m+2}$**, Phys. Rev. B **72**, 174113 (2005).

[2] D. M. Rowe, editor, **CRC Handbook of Thermoelectrics**, *CRC Handbook of Thermoelectrics*, Chemical Rubber Press, Boca Raton, FL, 1995.

[3] M. G. Kanatzidis, S. D. Mahanti, and T. P. Hogan, **Chemistry, Physics, and Materials Science of Thermoelectric Materials: Beyond Bismuth Telluride**, *Chemistry, Physics, and Materials Science of Thermoelectric Materials: Beyond Bismuth Telluride*, Kluwer Academic/Plenum Publishers, 2002.

[4] T. M. Tritt and M. A. Subramanian, **Thermoelectric materials, phenomena, and applications: A bird's eye view**, MRS Bulletin **31**, 188 (2006).

[5] G. S. Nolas, J. Sharp, and H. J. Goldsmid, **Thermoelectrics: basic principles and new materials developments**, *Thermoelectrics: basic principles and new materials developments*, Springer-Verlag, 2001.

[6] F. J. DiSalvo, **Thermoelectric cooling and power generation**, Science **285**, 703 (1999).

[7] G. A. Slack, **New materials and performance limits for thermoelectric cooling**, in *CRC Handbook of Thermoelectrics*, edited by D. M. Rowe, chapter 34, Chemical Rubber, Boca Raton, FL, 1995.

[8] G. A. Slack and V. G. Tsoukala, **Some properties of semiconducting $IrSb_3$**, J. Appl. Phys. **76**, 1665 (1994).

[9] G. S. Nolas, J. L. Cohn, and G. A. Slack, **Effect of partial void filling on the lattice thermal conductivity of skutterudites**, Phys. Rev. B **58**, 164 (1998).

[10] G. S. Nolas, J. L. Cohn, G. A. Slack, and S. B. Schujman, **Semiconducting Ge clathrates: promising candidates for thermoelectric applications**, Appl. Phys. Lett. **73**, 178 (1998).

[11] R. Venkatasubramanian, E. Siivola, T. Colpitts, and B. O'Quinn, **Thin-film thermoelectric devices with high room-temperature figures of merit**, Nature **413**, 597 (2001).

[12] L. D. Hicks and M. S. Dresselhaus, **Effect of quantum-well structures on the thermoelectric figure of merit**, Phys. Rev. B **47**, 12727 (1993).

[13] H. Beyer, J. Nurnus, H. Böttner, A. Lambrecht, E. Wagner, and G. Bauer, **High thermoelectric figure of merit ZT in PbTe and Bi2Te3-based superlattices by a reduction of the thermal conductivity**, Physica E **13**, 965 (2002).

[14] J. C. Caylor, K. Coonley, J. Stuart, T. Colpitts, and R. Venkatasubramanian, **Enhanced thermoelectric performance in PbTe-based superlattice structures from reduction of lattice thermal conductivity**, Appl. Phys. Lett. **87**, 023105 (2005).

[15] T. C. Harman, P. J. Taylor, M. P. Walsh, and B. E. LaForge, **Quantum dot superlattice thermoelectric materials and devices**, Science **297**, 2229 (2002).

[16] G. J. Snyder, M. Christensen, E. Nishibori, T. Caillat, and B. B. Iversen, **Disordered zinc in Zn_4Sb_3 with phonon-glass and electron-crystal thermoelectric properties**, Nat. Mater. **3**, 458 (2004).

[17] K. F. Hsu, S. Loo, F. Guo, W. Chen, J. S. Dyck, C. Uher, T. Hogan, E. K. Polychroniadis, and M. G. Kanatzidis, **Cubic $AgPb_mSbTe_{2+m}$: Bulk thermoelectric materials with high figure of merit**, Science **303**, 818 (2004).

[18] G. D. Mahan and J. O. Sofo, **The best thermoelectric**, Proc. Natl. Acad. Sci. USA **93**, 7436 (1996).

[19] T. J. Seebeck, **Magnetische Polarisation der Metalle und Erzedurch Temperatur-Differenz.Abhand**, Deut. Akad. Wiss. Berlin , 265 (1822).

[20] J. C. Peltier, **Nouvelles experiences sur la caloriecete des courans electriques**, Ann. Chem. **LVI**, 371 (1834).

[21] A. F. Ioffe, **Semiconductor thermoelements and thermoelectric cooling**, Infosearch, London (1957).

[22] W. Thomson, **On a mechanical theory of thermoelectric currents**, Proc. Roy. Soc., Edinburgh , 91 (1851).

[23] H. J. Goldsmid, **Applications of thermoelectricity**, *Applications of thermoelectricity*, Methuen, London, 1960.

[24] G. J. Snyder, web page The Science and Materials behind Thermoelectrics, URL: http://www.its.caltech.edu/~jsnyder/thermoelectrics/science_page.htm.

[25] E. Altenkirch, **Concerning the nutz effect on thermal columns**, Physikalische Zeitschrift **10**, 560 (1909).

[26] E. Altenkirch, **Electro-thermal generation of coldness and reversible electric heating**, Physikalische Zeitschrift **12**, 920 (1911).

[27] A. F. Ioffe, Poluprovodnikovye Termoelementy, Moskow-Leningrad (1956).

[28] G. J. Snyder and T. Ursell, **Thermoelectric efficiency and compatibility**, Phys. Rev. Lett. **91**, 148301 (2003).

[29] E. Quarez, K. F. Hsu, R. Pcionek, N. Frangis, E. K. Polychroniadis, and M. G. Kanatzidis, **Nanostructuring, compositional fluctuations, and atomic ordering in the thermoelectric materials $AgPb_mSbTe_{2+m}$. The myth of solid solutions**, J. Am. Chem. Soc. **127**, 9177 (2005).

[30] J. Androulakis, R. Pcionek, E. Quarez, J. H. Do, H. J. Kong, O. Palchik, C. Uher, J. J. D'Angelo, J. Short, T. Hogan, and M. G. Kanatzidis, **Coexistence of large thermopower and degenerate doping in the nanostructured material $Ag_{0.85}SnSb_{1.15}Te_3$**, Chem. Mater. **18**, 4719 (2006).

[31] J. Androulakis, K. F. Hsu, R. Pcionek, H. Kong, C. Uhr, J. J. D'Angelo, A. Downey, T. Hogan, and M. G. Kanatzidis, **Nanostructuring and high thermoelectric efficiency in p-Type $Ag(Pb_{1-y}Sn_y)_mSbTe_{2+m}$**, Adv. Mater. **18**, 1170 (2006).

[32] H. M. Rietveld, **A profile refinement method for nuclear and magnetic structures**, J. Appl. Crystallogr. **2**, 65 (1969).

[33] R. Prinz and D. Koningsberger, editors, **X-ray absorption: principles, applications techniques of EXAFS, SEXAFS and XANES**, *X-ray absorption: principles, applications techniques of EXAFS, SEXAFS and XANES*, J. Wiley and Sons, New York, 1988.

[34] S. P. Brown and L. Emsley, **Solid-State NMR**, in *Handbook of Spectroscopy*, edited by G. Gauglitz and T. Vo-Dinh, volume 2, Wiley, 2003.

[35] T. Egami and S. J. L. Billinge, **Underneath the Bragg peaks: structural analysis of complex materials**, *Underneath the Bragg peaks: structural analysis of complex materials*, Pergamon Press, Elsevier, Oxford, England, 2003.

[36] S. J. L. Billinge and M. G. Kanatzidis, **Beyond crystallography: the study of disorder, nanocrystallinity and crystallographically challenged materials**, Chem. Commun. , 749 (2004).

[37] L. P. Tarasov and B. E. Warren, **X-ray diffraction study of liquid sodium**, J. Chem. Phys. **4**, 236 (1936).

[38] B. E. Warren, H. Krutter, and O. Morningstar, **Fourier analysis of X-ray patterns of vitreous SiO_2 and B_2O_3**, J. Am. Ceram. Soc. **19**, 202 (1936).

[39] R. Kaplow, B. L. Averbach, and S. L. Strong, **Pair correlations in solid lead near the melting temperature**, J. Phys. Chem. Solids **25**, 1195 (1964).

[40] H. Ocken and C. N. J. Wagner, **Temperature dependence of the structure of liquid indium**, Phys. Rev. **149**, 122 (1966).

[41] B. Gilbert, F. Huang, H. Zhang, G. A. Waychunas, and J. F. Banfield, **Nanoparticles: Strained and Stiff**, Science **305**, 651 (2004).

[42] G. Paglia, E. S. Božin, and S. J. L. Billinge, **A novel fine-scale nanostructure in γ-Al_2O_3**, Chem. Mater. **18**, 3242 (2006).

[43] S. J. L. Billinge, **Real-space Rietveld: full profile structure refinement of the atomic pair distribution function**, in *Local Structure from Diffraction*, edited by S. J. L. Billinge and M. F. Thorpe, page 137, New York, 1998, Plenum.

[44] S. J. L. Billinge, **Local atomic structure and superconducivity of $Nd_{2-x}Ce_xCuO_{4-y}$: a pair distribution function study**, Ph.D Thesis,, 1992.

[45] S. J. L. Billinge, R. G. DiFrancesco, G. H. Kwei, J. J. Neumeier, and J. D. Thompson, **Direct observation of lattice polaron formation in the local structure of $La_{1-x}Ca_xMnO_3$**, Phys. Rev. Lett. **77**, 715 (1996).

[46] E. S. Božin, S. J. L. Billinge, H. Takagi, and G. H. Kwei, **Neutron diffraction evidence of microscopic charge inhomogeneities in the CuO_2 plane of superconducting $La_{2-x}Sr_xCu_4$ ($0 \leq x \leq 0.30$)**, Phys. Rev. Lett. **84**, 5856 (2000).

[47] E. S. Božin, S. J. L. Billinge, G. H. Kwei, and H. Takagi, **Charge-stripe ordering from local octahedral tilts: underdoped and superconducting $La_{2-x}Sr_xCuO_4$ ($0 \leq x \leq 0.3$)**, Phys. Rev. B **59**, 4445 (1999).

[48] E. S. Božin, S. J. L. Billinge, and G. H. Kwei, **Reexamination of the second order structural phase transition in $La_{2-x}A_xCuO_4$ (A=Ba,Sr)**, Physica B **241-243**, 795 (1998).

[49] V. Petkov, S. J. L. Billinge, T. Vogt, A. S. Ichimura, and J. L. Dye, **Structure of intercalated Cs in zeolite ITQ-4: an array of metal ions and electrons confined in a pseudo-1D nanoporous host**, Phys. Rev. Lett. **89**, 075502 (2002), (Highlighted in Phys. Rev. Focus: http://focus.aps.org/story/v10/st4).

[50] V. Petkov, P. N. Trikalitis, E. S. Božin, S. J. L. Billinge, T. Vogt, and M. G. Kanatzidis, **Structure of $V_2O_5.nH_2O$ xerogel solved by the atomic pair distribution function technique**, J. Am. Chem. Soc. **124**, 10157 (2002).

[51] V. Petkov, S. J. L. Billinge, P. Larson, S. D. Mahanti, T. Vogt, K. K. Rangan, and M. G. Kanatzidis, **Structure of nanocrystalline materials using atomic pair distribution function analysis: study of $LiMoS_2$**, Phys. Rev. B **65**, 092105 (2002).

[52] V. Petkov, S. J. L. Billinge, J. Heising, and M. G. Kanatzidis, **Application of atomic pair distribution function analysis to materials with intrinsic disorder. Three-dimensional structure of exfoliated-restacked WS_2: not just a random turbostratic assembly of layers**, J. Am. Chem. Soc. **122**, 11571 (2000).

[53] K. Furukawa, **The radial distribution curves of liquids by diffraction methods**, Rep. Prog. Phys. **25**, 395 (1962).

[54] B. E. Warren, **X-ray diffraction**, *X-ray diffraction*, Dover, New York, 1990.

[55] A. C. Wright, **Diffraction studies of glass structure: the first 70 years**, Glass. Phys. Chem. **24**, 148 (1998).

[56] V. Petkov, S. J. L. Billinge, S. D. Shastri, and B. Himmel, **Polyhedral units and network connectivity in calcium aluminosilicate glasses from high energy X-ray diffraction**, Phys. Rev. Lett. **85**, 3436 (2000).

[57] I.-K. Jeong, F. Mohiuddin-Jacobs, V. Petkov, S. J. L. Billinge, and S. Kycia, **Local structure study of $In_xGa_{1-x}As$ semiconductor alloys using high energy synchrotron X-ray diffraction**, Phys. Rev. B **63**, 205202 (2001).

[58] P. F. Peterson, T. Proffen, I. Jeong, S. J. L. Billinge, K.-S. Choi, M. G. Kanatzidis, and P. G. Radaelli, **Local atomic strain in $ZnSe_{1-x}Te_x$ from high real space resolution neutron pair distribution function measurements**, Phys. Rev. B **63**, 165211 (2001).

[59] R. L. McGreevy and P. Zetterstrom, **To RMC or not to RMC? The use of reverse Monte Carlo modelling**, Curr. Opin. Solid St. M. **7**, 41 (2003).

[60] M. G. Tucker, M. T. Dove, and D. A. Keen, **Application of the reverse Monte Carlo method to crystalline materials**, J. Appl. Crystallogr. **34**, 630 (2001).

[61] M. G. Tucker, M. P. Squires, M. T. Dove, and D. A. Keen, **Dynamic structural disorder in cristobalite: neutron total scattering measurement and reverse Monte Carlo modelling**, J. Phys.: Condens. Mat. **13**, 403 (2001).

[62] A. K. Soper, **Tests of the empirical potential structure refinement method and a new method of application to neutron diffraction data on water**, Mol. Phys. **99**, 1503 (2001).

[63] A. K. Soper, **The radial distribution functions of water and ice from 220 to 673 K and at pressures up to 400 MPa**, Chem. Phys. **258**, 121 (2000).

[64] X. Qiu, E. S. Božin, P. Juhas, T. Proffen, and S. J. L. Billinge, **Reciprocal space instrumental effects on the real space neutron atomic pair distribution function**, J. Appl. Crystallogr. **37**, 110 (2004).

[65] T. Proffen and S. J. L. Billinge, **PDFFIT, a program for full profile structural refinement of the atomic pair distribution function**, J. Appl. Crystallogr. **32**, 572 (1999).

[66] C. L. Farrow, P. Juhas, J. W. Liu, D. Bryndin, J. Bloch, T. Proffen, and S. J. L. Billinge, **PDFfit2 and PDFgui: Computer programs for studying nanostructure in crystals**, J. Phys: Condens. Matter (2006), submitted.

[67] P. J. Chupas, X. Qiu, J. C. Hanson, P. L. Lee, C. P. Grey, and S. J. L. Billinge, **Rapid acquisition pair distribution function analysis (RA-PDF)**, J. Appl. Crystallogr. **36**, 1342 (2003).

[68] X. Qiu, J. W. Thompson, and S. J. L. Billinge, **PDFgetX2: a GUI driven program to obtain the pair distribution function from X-ray powder diffraction data**, J. Appl. Crystallogr. **37**, 678 (2004).

[69] K. Takahashi, K. Kohda, J. Miyahara, Y. Kanemitsu, K. Amitani, and S. Shionoya, **Mechanism of photostimulated luminescence in BaFCl$^-$Eu^{2+}, BaFBr$^-$Eu^{2+} phosphors**, Journal Of Luminescence **31-2**, 266 (1984).

[70] K. Takahashi, **Progress in science and technology on photostimulable BaFX : Eu^{2+} (X = Cl, Br, I) and imaging plates**, Journal of Luminescence **100**, 307 (2002).

[71] H. Vonseggern, T. Voigt, W. Knupfer, and G. Lange, **Physical model of photostimulated luminescence of X-ray-irradiated BaFBr:Eu^{2+}**, J. Appl. Phys. **64**, 1405 (1988).

[72] Y. Amemiya, **Imaging plates for use with synchrotron-radiation**, J. Synchrotron Rad. **2**, 13 (1995).

[73] Y. Iwabuchi, C. Umemoto, K. Takahashi, and S. Shionoya, **Photostimulated luminescence process in BaFBr$^-$Eu^{2+} containing F(Br$^-$) and F(F$^-$) centers**, Journal of Luminescence **48-9**, 481 (1991).

[74] J. Miyahara, K. Takahashi, Y. Amemiya, N. Kamiya, and Y. Satow, **A new type of X-ray area detector utilizing laser stimulated luminescence**, Nucl. Instrum. Methods A **246**, 572 (1986).

[75] Y. Amemiya, T. Matsushita, A. Nakagawa, Y. Satow, J. Miyahara, and J. Chikawa, **Design and performance of an imaging plate system for X-ray-diffraction study**, Nucl. Instrum. Methods A **266**, 645 (1988).

[76] Y. Amemiya, S. Kishimoto, T. Matsushita, Y. Satow, and M. Ando, **Imaging plate for time-resolved X-ray measurements**, Rev. Sci. Instrum. **60**, 1552 (1989).

[77] A. P. Hammersley, **FIT2D v9.129 reference manual v3.1**, ESRF Internal Report ESRF98HA01T, 1998.

[78] $ZT = \sigma S^2 T/\kappa$, where T is the operating temperature of the device, S is the thermopower, and σ and κ are the electrical and thermal conductivities of the material, respectively.

[79] Z. H. Dughaish, **Lead telluride as a thermoelectric material for thermoelectric power generation**, Physica B **322**, 205 (2002).

[80] H. Beyer, J. Nurnus, H. Böttner, and A. Lambrecht, **PbTe based superlattice structures with high thermoelectric efficiency**, Appl. Phys. Lett. **80**, 1216 (2002).

[81] D. Bilc, S. D. Mahanti, K.-F. Hsu, E. Quarez, R. Pcionek, and M. G. Kanatzidis, **Resonant states in the electronic structure of the high performance thermoelectrics $AgPb_mSbTe_{2+m}$: The role of Ag-Sb microstructures**, Phys. Rev. Lett. **93**, 146403 (2004).

[82] T. E. Humphrey and H. Linke, **Reversible Thermoelectric Nanomaterials**, Phys. Rev. Lett. **94**, 096601 (2005).

[83] S. Vensky, L. Kienle, R. E. Dinnebier, A. S. Masadeh, S. J. L. Billinge, and M. Jansen, **The real structure of Na_3BiO_4 by electron microscopy, HR-XRD and PDF analysis**, Z. Kristallogr. **220**, 231 (2005).

[84] J. Bloch, T. Proffen, and S. J. L. Billinge, **PDFFIT2; an updated C++ implementation of the PDFFIT program**, unpublished, 2005.

[85] S. Geller and J. H. Wernick, **Ternary semiconducting compounds with sodium chloride structure: $AgSbSe_2$, $AgSbTe_2$, $AgBiS_2$, $AgBiSe_2$**, Acta Crystallogr. **12**, 46 (1959).

[86] K. Hoang, K. Desai, and S. D. Mahanti, **Charge ordering and self-assembled nanostructures in a fcc Coulomb lattice gas**, Phys. Rev. B **72**, 064102 (2005).

[87] D. Bilc, S. D. Mahanti, and M. G. Kanatzidis, **Electronic transport properties of PbTe and $AgPb_mSbTe_{2+m}$ systems**, Phys. Rev. B **74**, 125202 (2006).

[88] W. Kim, J. Zide, A. Gossard, D. Klenov, S. Stemmer, A. Shakouri, and A. Majumdar, **Thermal conductivity reduction and thermoelectric figure of merit increase by embedding nanoparticles in crystalline semiconductors**, Phys. Rev. Lett. **96**, 045901 (2006).

[89] J. Androulakis, C. H. Ling, R. Pcionek, H. Kong, C. Uher, T. Hogan, B. Cook, T. Caillat, K. M. Paraskevopoulos, and M. G. Kanatzidis, submitted (2006).

[90] L. Vegard, **The constitution of the mixed crystals and the filling of space of the atoms**, Z. Phys. **5**, 17 (1921).

[91] M. F. Thorpe and E. J. Garboczi, **Elastic properties of central-force networks with bond-length mismatch**, Phys. Rev. B **42**, 8405 (1990).

[92] V. Petkov, I-K. Jeong, J. S. Chung, M. F. Thorpe, S. Kycia, and S. J. L. Billinge, **High real-space resolution measurement of the local structure of $Ga_{1-x}In_xAs$ using X-ray diffraction**, Phys. Rev. Lett. **83**, 4089 (1999).

[93] J. W. Cahn, **On spinodal decomposition**, Acta Matall. Mater. **9**, 795 (1961).

[94] M. S. Darrow, W. B. White, and R. Roy, **Phase Relations in the System PbS-PbTe**, T. Metall. Soc. AIME **236**, 654 (1966).

[95] V. Leute and N. Volkmer, **A Contribution to the Phase Diagram of the Quasibinary System $PbS_{1-x}Te_x$."**, Z. Phys. Chem. Neue Fol. **144**, 145 (1985).

[96] T. C. Harman, M. P. Walsh, B. E. LaForge, and G. W. Turner, **Nanostructured thermoelectric materials**, J. Electron. Mater. **34**, L19 (2005).

[97] S. Yamamoto, Sci. Rep. Res. Tohoku U., First Ser. **40**, 11 (1956).

[98] N. D. Sindeyeva and A. A. Godovikov, Dokl. Akad. Nauk SSSR **127**, 431 (1959).

[99] A. Y. Malevskiy, Dokl. Akad. Nauk SSSR **152**, 191 (1963).

[100] P. F. Peterson, E. S. Božin, T. Proffen, and S. J. L. Billinge, **Improved measures of quality for atomic pair distribution functions**, J. Appl. Crystallogr. **36**, 53 (2003).

[101] A. A. Coelho, TOPAS General Profile and Structure Analysis Software for Powder Diffraction Data; http://members.optusnet.com.au/~alancoelho/, 2004.

[102] P. E. Werner, S. Salome, G. Malmros, and J. O. Thomas, **Quantitative analysis of multicomponent powders by full-profile refinement of Guinier-Hägg X-ray film data**, J. Appl. Crystallogr. **12**, 107 (1979).

[103] R. J. Hill and C. J. Howard, **Quantitative phase-analysis from neutron powder diffraction data using the Rietveld method**, J. Appl. Crystallogr. **20**, 467 (1987).

[104] D. L. Bish and S. A. Howard, **Quantitative phase-analysis using the Rietveld method**, J. Appl. Crystallogr. **21**, 86 (1988).

[105] B. H. O'Connor and M. D. Raven, **Application of the Rietveld refinement procedure in assaying powdered mixtures**, Powder Diffr. **3**, 2 (1988).

[106] R. J. Hill, **Expanded use of the Rietveld method in studies of phase abundance in multiphase mixtures**, Powder Diffr. **6**, 74 (1991).

[107] R. A. Young, **The Rietveld Method**, *The Rietveld Method*, volume 5 of *International Union of Crystallography Monographs on Crystallography*, Oxford University Press, Oxford, 1993.

[108] T. Proffen, V. Petkov, S. J. L. Billinge, and T. Vogt, **Chemical short range order obtained from the atomic pair distribution function**, Z. Kristallogr. **217**, 47 (2002).

[109] Y. Noda, K. Masumoto, S. Ohba, Y. Saito, K. Toriumi, Y. Iwata, and I. Shibuya, **Temperature Dependence of Atomic Thermal Parameters of Lead Chalcogenides, PbS, PbSe and PbTe**, Acta Crystallogr. C **43**, 1443 (1987).

[110] I.-K. Jeong, T. Proffen, F. Mohiuddin-Jacobs, and S. J. L. Billinge, **Measuring correlated atomic motion using X-ray diffraction**, J. Phys. Chem. A **103**, 921 (1999).

[111] C. Farrow, **EXAFS analysis of $La_{0.70}Ca_{0.30}MnO_3$ and $Ag_{0.86}SbPb_{18}Te_{20}$**, unpublished, 2006.

[112] P. H. Fuoss, P. Eisenberger, W. K. Warburton, and A. I. Bienenstock, **Application of differential anomalous x-ray-scattering to structural studies of amorphous materials**, Phys. Rev. Lett. **46**, 1537 (1981).